

Manuscript Details

Manuscript number	ADWR_2017_628_R2
Title	Simultaneous identification of a contaminant source and hydraulic conductivity via the restart normal-score ensemble Kalman filter
Article type	Research Paper

Abstract

Detecting where and when a contaminant entered an aquifer from observations downgradient of the source is a difficult task; this identification becomes more challenging when the uncertainty about the spatial distribution of hydraulic conductivity is accounted for. In this paper, we have implemented an application of the restart normal-score ensemble Kalman filter (NS-EnKF) for the simultaneous identification of a contaminant source and the spatially variable hydraulic conductivity in an aquifer. The method is capable of providing estimates of the spatial location, initial release time, the duration of the release and the mass load of a point-contamination event, plus the spatial distribution of hydraulic conductivity together with an assessment of the estimation uncertainty of all the parameters. The method has been applied in synthetic aquifers exhibiting both Gaussian and non-Gaussian patterns. The identification is made possible by assimilating in time both piezometric head and concentration observations from an array of observation wells. The method is demonstrated in three different synthetic scenarios that combine hydraulic conductivities with unimodal and bimodal histograms, and releases in high and low conductivity zones. The results prove that the specific implementation of the EnKF is capable of recovering the source parameters with some uncertainty and of recovering the main patterns of heterogeneity of the hydraulic conductivity fields by assimilating a sufficient number of state variable observations. The proposed approach is an important step towards contaminant source identification in real aquifers, which may have logconductivity spatial distributions with either Gaussian or non-Gaussian features, yet, it is still far from practical applications since the transport parameters, the external sinks and sources and the initial and boundary conditions are assumed known.

Keywords	Contaminant source identification; restart Ensemble Kalman filter; Heterogeneity; Normal-score transform
Taxonomy	Contaminant Fate in Groundwater, Inverse Problem, Geostatistics, Groundwater Models, Inverse Hydrological Modeling
Corresponding Author	Teng Xu
Corresponding Author's Institution	Universitat Politècnica de València
Order of Authors	Teng Xu, J. Jaime Gomez-Hernandez
Suggested reviewers	Andrea Zanini, Liangping Li, Xiaodong Luo, Harrie-Jan Hendricks Franssen, Haiyan Zhou

Submission Files Included in this PDF

File Name [File Type]

paper_coverletter.pdf [Cover Letter]

Response to Reviewers_ADWR_Rev1.doc [Response to Reviewers]

Research_highlights.docx [Highlights]

work_9.pdf [Manuscript File]

Submission Files Not Included in this PDF

File Name [File Type]

ADWR_dispersivity_revision2.zip [LaTeX Source File]

To view all the submission files, including those not included in the PDF, click on the manuscript title on your EVISE Homepage, then click 'Download zip file'.

Research Data Related to this Submission

There are no linked research data sets for this submission. The following reason is given:
Data will be made available on request

Simultaneous identification of a contaminant source and hydraulic conductivity via the restart normal-score ensemble Kalman filter

Teng Xu ¹
J. Jaime Gómez-Hernández ²

*Group of Hydrogeology
Universidad Politécnica de Valencia
Camino de Vera, s/n, 46022, Valencia, Spain
Tel. (34) 963879615
Fax. (34) 963879492*

Submitted to
Advances in Water Resources
July 28, 2017

¹corresponding author. E-mail: tenxu@posgrado.upv.es

²E-mail: jaime@dihma.upv.es

Comments of editor and reviewers from the ADWR

We thank again the associate editor and the reviewers for their comments. We have addressed their concerns in our revision of the original manuscript. The major change, in response to the comments, has been the softening of the claim of novelty as requested by reviewer 3.

Dear Dr Xu,

We received now two re-reviews for your paper "Simultaneous identification of a contaminant source and hydraulic conductivity via the restart normal-score ensemble Kalman Filter". One of the two original reviewers finds that his/her comments are only handled partly and asks you to consider again making some changes to the manuscript. In particular, the claim of novelty of the paper should be somewhat relaxed. I suggest that you will again have the chance to make some final improvements and corrections to the paper and recommend the editor minor revision.

Looking forward to the revised version of your paper.

Best regards,

Associate Editor

-Reviewer 2

All my comments have been addressed satisfactorily and the paper is ready to be published. The new simulation reported in the appendix, in particular, is useful and fully addressed my previous main comment. Perhaps the appendix should appear as supplementary information, but I guess the copyediting staff will decide this. See also a few minor corrections below

Line 31: replace "an nonlinear" with "a nonlinear".

Lines 189-191: knowledge of the marginal distributions and training images represents already all the prior information needed. I suggest the sentence be replaced with "They are unconditional realizations based on their marginal distributions and the training image for S2 and S3".

Line 263: replace "what explains that" with "which explains why".

The three editorial changes suggested by the reviewer have been incorporated.

-Reviewer 3

- The authors have replied to all of my comments by either addressing them in the revised manuscript or by explaining why they chose not to. The revised manuscript is now more convincing in some parts, although I would have hoped for an even stronger effect. Most of the not-addressed points are a matter of intended readership, others are more critical (see specific comments below). Overall, I suggest to send the manuscript back to the authors for a final minor revision.

- The authors point to several previous works where performance and technical details of the NS-EnKF had been discussed. Of course this material exists and readers can refer to it, but from a methodological point of view a manuscript is even more valuable if it is able to provide a brief synthesis of previous and current results and to highlight most important differences or similarities. The authors chose not to do this in detail, which will have an effect on who is benefitting most from reading this paper (and the impact of the paper in general), but of course the intended readership is in the responsibility of the authors.

We maintain our view that the additional references included in the revised manuscript should be enough for any interest reader to go deeper into the performance of the NS-EnKF

- The same holds for the comparison with a deterministic K-field: Of course this is not the case in reality, but from a methodological point of view, such a comparison could be interesting to highlight even more the importance of simultaneous identification.

As mentioned in our reply, this study was performed on a previous study by us. We do not see the need to repeat it here.

- With respect to the number of figures: In draft mode, the manuscript now has as many pages of text as of figures/tables. In my view, there is a misbalance, but this is finally up to the authors and editors.

We believe in the aphorism that a picture is worth a thousand words, and that all the figures included are important to understand the performance of the approach on the different scenarios

- Most problematic is the claim of novelty:

L. 39 – 44: “Koch and Nowak [20] combined a stochastic multiphase model and a reverse transport formulation within an inverse Bayesian methodology for the joint inversion of contaminated source zone architectures and aquifer parameters. However, in all of those studies, the aquifers analyzed are either homogeneous, or, at most divided in a few homogeneous subzones. To the best of our knowledge, no approach has been proposed capable to handle the simultaneous identification of a contaminant source and the conductivities in a truly heterogeneous aquifer.” This is not true, Koch and Nowak use a Bayesian geostatistical framework to simulate and infer heterogeneous aquifer parameters.

We have rewritten the text to give credit to Koch and Nowak for having done already simultaneous identification of aquifer parameters and source information.

This may be a first-time application of the NS-EnKF to the joint inversion, but not a first-time joint inversion of permeability and source zone parameters. The

authors need to clearly define the novelty of their work and to carefully rephrase their statements in the abstract and throughout the manuscript accordingly. Finally, I thank the authors for mentioning my reviewing activity in the acknowledgments; however I do not insist to be mentioned since my suggested input is not reflected in the revised manuscript to such a notable degree.

We have removed the explicit reference to the reviewer in the acknowledgments.

- Contaminant source parameters and heterogeneous conductivity field can be jointly identified using the EnKF by assimilating enough observation data.
- Three synthetic scenarios in two different heterogeneous aquifers are used to test the joint parameter identification.
- The analysis for the results of the three scenarios proves the ability of the EnKF in the joint parameter identification.

Simultaneous identification of a contaminant source and hydraulic conductivity via the restart normal-score ensemble Kalman filter

Teng Xu^{a,*}, J. Jaime Gómez-Hernández^a

^a*Research Institute of Water and Environmental Engineering, Universitat Politècnica de València, 46022, Valencia, Spain*

Abstract

Detecting where and when a contaminant entered an aquifer from observations downgradient of the source is a difficult task; this identification becomes more challenging when the uncertainty about the spatial distribution of hydraulic conductivity is accounted for. In this paper, we have implemented an application of the restart normal-score ensemble Kalman filter (NS-EnKF) for the simultaneous identification of a contaminant source and the spatially variable hydraulic conductivity in an aquifer. The method is capable of providing estimates of the spatial location, initial release time, the duration of the release and the mass load of a point-contamination event, plus the spatial distribution of hydraulic conductivity together with an assessment of the estimation uncertainty of all the parameters. The method has been applied in synthetic aquifers exhibiting both Gaussian and non-Gaussian patterns. The identification is made possible by assimilating in time both piezometric head and concentration observations from an array of observation wells. The method is demonstrated in three different synthetic scenarios that combine hydraulic conductivities with unimodal and bimodal histograms, and releases in high and low conductivity zones. The results prove that the specific implementation of the EnKF is capable of recovering the source parameters with some uncertainty and of recovering the main patterns of heterogeneity of the hydraulic conductivity fields by assimilating a sufficient number of state variable observations. The proposed approach is an important step towards contaminant source identification in real aquifers, which may have logconductivity spatial distributions with either Gaussian or non-Gaussian features, yet, it is still far from practical applications since the transport parameters, the external sinks and sources and the initial and boundary conditions are assumed known.

Keywords: Contaminant source identification, restart Ensemble Kalman filter, Heterogeneity, Normal-score transform

*Corresponding author: Teng Xu Tel: +34 963879615 Fax: +34 963879492
Email addresses: tenxu@posgrado.upv.es (Teng Xu), jaime@dihma.upv.es (J. Jaime Gómez-Hernández)

1. Introduction

Groundwater movement is slow and often a contamination plume may reach a water supply well when the source has disappeared; or a contaminant may enter an aquifer unnoticed, i.e., from a leaky underground storage tank, and when the contaminant is detected, nobody knows exactly its origin. Could the source be identified from the time series of concentrations observed in one or several downstream wells from the release point? This is a question that many researchers have posed and which has been studied in the past decades. The vast majority of all previous approaches are based on some sort of optimization of an objective function that measures deviations between model predictions and observations, with the source location and release time as the parameters to identify. For example, Gorelick et al. [1] used least-squares regression and linear programming combined with contaminant transport simulation to identify a pollutant source location; Sun et al. [2] proposed a constrained robust least squares approach (CRLS) for contaminant release history identification and then used the CRLS estimator combined with a branch-and-bound global optimization for iteratively identifying source release histories and source locations [3]; Aral et al. [4] proposed a progressive genetic algorithm in the context of nonlinear optimization; Yeh et al. [5, 6] combined simulated annealing and tabu search; Mirghani et al. [7] employed a simulation-optimization approach that uses an evolutionary search algorithm; Dokou and Pinder [8] developed an optimal search strategy for source location identification; Amirabdollahian and Datta [9] designed an optimal source identification model using Adaptive Simulated Annealing to identify the contaminant source; Ayvaz [10] proposed a hybrid simulation-optimization approach for solving the areal groundwater pollution source identification problem. Some approaches are not based on optimization; for instance, Butera et al. [11], Cupola et al. [12] employed a Bayesian geostatistical approach to identify the source location, after a preliminary delineation of a probable source area; and Gzyl et al. [13] used a quasilinear geostatistical methodology to identify the source location from some suspect contamination sources.

All the studies mentioned above mainly focus on the identification of source location information in a deterministic aquifer where the aquifer properties are assumed perfectly known. There are a few studies carried out for the simultaneous identification of contaminant source information and aquifer properties. Wagner [14] used non-linear maximum likelihood combined with groundwater flow and contaminant transport simulation for the estimation of flow parameters in a two-zone aquifer and the source parameters. Sidauruk et al. [15] developed inverse procedures based on optimizing correlation coefficients to locate ground water contaminant sources and to identify transport parameters of a homogeneous aquifer. Mahar and Datta [16] used a nonlinear optimization model where the flow and transport equations are embedded as constraints to estimate the

119
120
121
122 32 magnitude, location and duration of a groundwater pollution source and later [17] they extended the method
123 33 to include the simultaneous estimation of aquifer parameters in a homogeneous and isotropic aquifer system.
124 34 Singh and Datta [18] utilized a trained artificial neural network to simultaneously estimate a groundwater
125 35 contaminant source and to estimate the hydraulic conductivity, porosity, and dispersivity of a homogeneous
126 36 aquifer. Datta et al. [19] presented a methodology using a combined optimization-simulation approach for
127 37 simultaneously identifying a contaminant source and estimating aquifer homogeneous parameters, where the
128 38 methodology links an optimization method to a groundwater flow and transport simulator as an external
129 39 module. Koch and Nowak [20] combined a stochastic multiphase model and a reverse transport formulation
130 40 within an inverse Bayesian methodology for the joint inversion of contaminated source zone architectures
131 41 and aquifer parameters.

132 42 However, with the exception of the work by Koch and Nowak Koch and Nowak [20], in all of those
133 43 studies, the aquifers analyzed are either homogeneous, or, at most divided in a few homogeneous subzones.
134 44 In a previous paper [21], we proposed the use of the ensemble Kalman filter (EnKF) —more precisely, its
135 45 variant, the restart normal-score EnKF (NS-EnKF), which has proven to be a very efficient inverse modeling
136 46 algorithm [e.g., 22, 23, 24, 25]— for contaminant source identification in a heterogeneous but deterministic
137 47 aquifer, and we ended the paper with the conclusion that although the NS-EnKF performed very well for
138 48 contaminant source identification, its application to a deterministic aquifer was unrealistic since detailed
139 49 aquifer heterogeneity will never be available in a practical case. In this paper, recognizing the importance of
140 50 proper characterization of conductivity for solute transport prediction [e.g., 26, 27], we move one step further
141 51 and we demonstrate the applicability of the NS-EnKF for the simultaneous identification of a heterogeneous
142 52 conductivity field and the parameters defining the source of a point contamination by assimilating in time
143 53 piezometric heads and solute concentrations. We must recognize upfront, that the rest of parameters and
144 54 variables controlling flow are assumed known, i.e., initial conditions, boundary conditions, and external
145 55 stresses, as well as the parameters controlling transport, which are considered homogeneous and known;
146 56 yet, the proposed methodology brings us closer to its application in a realistic setting from what had been
147 57 proposed in the past in the literature.

148 58 Next, the paper describes the proposed algorithm and continues with an application of the restart NS-
149 59 EnKF for three scenarios in two different heterogenous synthetic aquifers. The paper ends with a summary
150 60 and discussion, followed by an Appendix in which an extra scenario is discussed.

2. Ensemble Kalman filter

The EnKF proposed by Evensen [28] is the evolution of the Kalman filter to handle nonlinear transfer functions. It is based on using an ensemble of realizations to approximate the covariances and cross-covariances of parameters and state variables needed during the updating step of the Kalman filter. In recent years, the EnKF has received much attention for its efficiency and effectiveness in dealing with large dimensions and it has been widely applied in many fields, such as oceanography, meteorology, petroleum engineering, or hydrology [e.g., 29, 30, 31, 32, 23, 33].

Briefly, recall that the Kalman filter is an assimilation technique that updates the state and the parameters of the system sequentially in time as new state data are collected. The update is proportional to the deviations between the state forecast and the state observations at a few locations; in the ensemble Kalman filter, this update is heterogeneous in space and different for each member of the ensemble of realizations. In our case, the state variables are piezometric head (H) and solute concentration (C), and the parameters to update are hydraulic conductivity (K) and contaminant source information including location (X for the x-coordinate, Y for the y-coordinate), initial release time (T), release duration (ΔT), and solute mass-loading rate (M). Next, we detail the specific implementation of the restart NS-EnKF, which, like all the Kalman filter-based approaches, consists of two steps: forecast and analysis.

In the forecast step, state variables are forecasted into the next time step. Commonly, this forecast is done from the state estimate after the last updating time step; however, for the contaminant source identification, as was explained by Xu and Gómez-Hernández [21], Camporese et al. [34, 35], Crestani et al. [36, 37], it is necessary to make the forecast from time zero, since the contaminant source parameters refer to the source at time zero. This restart of the simulation after each time step, which is mandatory for the purpose of identifying the contaminant source, gives the name of “restart” NS-EnKF to the algorithm. Therefore, at each time step, the forecast of piezometric heads and concentrations is done from time zero until the end of the t^{th} time step (C_t, H_t) based on the concentrations and heads at time zero (C_0, H_0) and on the last updates of the source information and of the conductivity field at the $(t-1)^{\text{th}}$ time step ($X_{t-1}, Y_{t-1}, T_{t-1}, \Delta T_{t-1}, M_{t-1}, K_{t-1}$). The forecast uses a state transfer equation ψ , which is non other than a combined groundwater flow and contaminant transport model,

$$(C_t, H_t) = \psi(C_0, H_0, X_{t-1}, Y_{t-1}, T_{t-1}, \Delta T_{t-1}, M_{t-1}, K_{t-1}). \quad (1)$$

In the demonstration examples, we assume that the system is under transient conditions (both for ground-

237
 238
 239 water flow and for contaminant transport) and that only advection and dispersion are considered as transport
 240 mechanisms. The governing equations of the transient groundwater flow and contaminant transport are given
 241 in Eq. (2) [38] and Eq. (3) [39], respectively:
 242
 243

$$244 \quad S_s \frac{\partial H}{\partial t} - \nabla \cdot (K \nabla H) = W, \quad (2)$$

$$245 \quad \frac{\partial(\theta C)}{\partial t} = \nabla \cdot [\theta(D_m + \alpha v) \cdot \nabla C] - \nabla \cdot (\theta v C) - q_s C_s. \quad (3)$$

246
 247
 248 where S_s denotes specific storage [L^{-1}], H is the hydraulic head [L]; t is time [T]; $\nabla \cdot$ is the divergence
 249 operator; ∇ is the gradient operator; K is the hydraulic conductivity [LT^{-1}]; W denotes sources and sinks
 250 per unit volume [T^{-1}]. C is aqueous concentration [ML^{-3}], θ is the effective porosity of the aquifer sediment
 251 [-]. D_m is the molecular diffusion coefficient [L^2T^{-1}], α is the dispersivity tensor [L], v is the flow velocity
 252 vector [LT^{-1}], which is related to the specific discharge through, $v = -\frac{K}{\theta} \nabla H$; q_s is the volumetric flow rate
 253 per unit volume of the aquifer representing fluid sources or sinks [T^{-1}], and C_s is the concentration of the
 254 source or sink flux [ML^{-3}].
 255
 256
 257
 258
 259
 260
 261

262 The groundwater flow simulator MODFLOW [40] is used to solve Eq. (2), and the resulting flow velocity
 263 field (v) is used as input in Eq. (3), which is solved with the transport simulator MT3DMS [e.g., 39, 41].
 264

265 Note that although the EnKF can handle nonlinearities, it still fails to characterize non-Gaussian param-
 266 eters. To solve this problem and take advantage of the optimality of the EnKF for parameter identification
 267 under Gaussian conditions, several techniques, such as Gaussian mixture model, reparameterization, and
 268 normal-score transform (also referred to in the literature as Gaussian anamorphosis) have been employed in
 269 combination with the EnKF [e.g., 42, 43, 44]. The normal-score EnKF (NS-EnKF), as described by Zhou
 270 et al. [44], is one of the alternatives based on the use of a Gaussian anamorphosis to transform the parameters
 271 being identified into (univariate) Gaussian deviates [e.g., 45, 46, 23]. In this paper, we use this approach to
 272 handle the non-Gaussian parameters.
 273
 274
 275
 276
 277

278 The source contamination parameters ($X_{t-1}, Y_{t-1}, T_{t-1}, \Delta T_{t-1}, M_{t-1}$) and the conductivities K_{t-1} are
 279 all transformed into Gaussian deviates by using a specific normal-score transform for each parameter,
 280
 281
 282
 283
 284
 285
 286
 287
 288
 289
 290
 291
 292
 293
 294
 295

$$\begin{pmatrix} \tilde{X}_{t-1} \\ \tilde{Y}_{t-1} \\ \tilde{T}_{t-1} \\ \tilde{\Delta T}_{t-1} \\ \tilde{M}_{t-1} \\ \tilde{K}_{t-1} \end{pmatrix} = \begin{pmatrix} \phi_{X,t}(X_{t-1}) \\ \phi_{Y,t}(Y_{t-1}) \\ \phi_{T,t}(T_{t-1}) \\ \phi_{\Delta T,t}(\Delta T_{t-1}) \\ \phi_{M,t}(M_{t-1}) \\ \phi_{K,t}(K_{t-1}) \end{pmatrix}, \quad (4)$$

where $\phi_{X,t}$, $\phi_{Y,t}$, $\phi_{T,t}$, $\phi_{\Delta T,t}$, $\phi_{M,t}$, $\phi_{K,t}$ are the normal-score transform functions.

The prediction step in the NS-EnKF refers to the prediction of the normal-scored transformed variables from the normal-scored updated values at the last time step. Such a prediction involves the back-transformation of the updated normal scores followed by the forward modeling of flow and transport using Eq. (2) and (3) and then the transformation of the model results into normal scores.

In the analysis step, the EnKF will update the last estimate of the (normal-scored) parameters based on the discrepancy between the forecasted state variable values and the observed ones. The details of the normal-score EnKF can be looked up elsewhere [e.g., 44]. We simply summarize here that there is an ensemble of augmented vectors containing parameters and state variables, each vector of the ensemble can be split in two, a vector of parameters S (in our case, the normal-scored values in Eq. (5)), and a vector of states V (in our case, the piezometric heads and solute concentrations in Eq. (6)),

$$S = \begin{bmatrix} \tilde{X} \\ \tilde{Y} \\ \tilde{T} \\ \tilde{\Delta T} \\ \tilde{M} \\ \tilde{K} \end{bmatrix}, \quad (5)$$

$$V = \begin{bmatrix} C \\ H \end{bmatrix}. \quad (6)$$

From the ensembles of both vectors, compute the experimental state covariance (D_{VV}) for all pairs of locations with observational data, and the experimental state-parameter cross-covariance for all pairs of normal-scored parameter values and observational data (D_{SV}). Once the experimental covariances are

355
356
357 computed, the normal-scored parameters are updated using the following equation:
358
359

$$360 \quad S_t = S_{t-1} + G_t(V_t^o + e_t - V_t^{f,o}) \quad (7)$$

361
362
363 with

$$364 \quad G_t = D_{SV}(D_{VV} + R_t)^{-1}, \quad (8)$$

365
366 where S_t contains the updated normal-scored parameters, G_t is the Kalman gain matrix, V_t^o is the vector of
367 observed concentrations and observed heads, $V_t^{f,o}$ is the vector of forecasted concentrations and forecasted
368 heads at the observation locations, and e_t is an observation error with mean zero, standard deviation of 0.05,
369 and diagonal covariance R_t . Notice that the update is proportional to the departure between observed V_t^o and
370 forecasted state variables $V_t^{f,o}$ (at observation locations), with the Kalman gain G_t being the proportionality
371 factor. The Kalman gain (Eq. (8)) is proportional to the degree of correlation between state data and
372 parameters as measured by the cross-covariance D_{SV} , and inverse proportional to the redundancy of the
373 observed states as measured by the auto-covariance D_{VV} .
374
375
376
377
378

379 After all the normal-scored parameters are updated, back transform them into parameter space using
380 the inverse of the normal-score functions (see Equation Eq. (9)),
381
382

$$383 \quad \begin{pmatrix} X_t \\ Y_t \\ T_t \\ \Delta T_t \\ M_t \\ K_t \end{pmatrix} = \begin{pmatrix} \phi_{X,t}^{-1}(\tilde{X}_t) \\ \phi_{Y,t}^{-1}(\tilde{Y}_t) \\ \phi_{T,t}^{-1}(\tilde{T}_t) \\ \phi_{\Delta T,t}^{-1}(\tilde{\Delta T}_t) \\ \phi_{M,t}^{-1}(\tilde{M}_t) \\ \phi_{K,t}^{-1}(\tilde{K}_t) \end{pmatrix}. \quad (9)$$

393 3. Application

394
395 Two synthetic confined aquifers are built: one has a unimodal conductivity distribution; the other has a
396 bimodal conductivity distribution with strong continuity of the values around the larger mode of the two,
397 mimicking a channelized geology. Both aquifers are modeled as confined and discretized into 50 by 50 by
398 1 cells. (No units are reported throughout the paper since the results are insensitive to the units used as
399 long as all quantities have coherent units. Absolute magnitudes are not important, what is important are
400 relative values, such as the number of orders of magnitude of variability of the conductivity, the relative size
401
402
403
404
405
406
407
408
409
410
411
412
413

414 of the heterogeneity features with respect to the aquifer size, or the size of the plume within the aquifer for
415 the length of the simulation period. Physical dimensions are given in square brackets when a variable or
416 parameter appears for the first time.) Each cell is 1 [L] by 1 [L] by 5 [L].
417

418 Conductivities in both aquifers are heterogeneous. The reference log-conductivity field of the unimodal
419 aquifer (see Figure 1) is generated with GCOSIM3D [47] from a Gaussian distribution with the parameters
420 shown in the first row of Table 1. The channelized aquifer consists of 35% high conductivity channel
421 values and 65% low conductivity non-channel medium. The procedure for the generation of the reference
422 log-conductivity field is as follows: first, generate a binary facies map using the SNESIM code [48] with the
423 training image in Figure 2, and then populate each facies with log-conductivity values from two multiGaussian
424 distributions with the parameters shown in the last two rows of Table 1, each facies is generated independently
425 with the code GCOSIM3D. The resulting reference log-conductivity field of the channelized aquifer is shown
426 in Figure 1 with a global mean of $-1.2 [\ln(LT^{-1})]$ and a global standard deviation of $1.9 [\ln(LT^{-1})]$.
427

428 In both aquifers, boundaries are impermeable, and there are 2 injection wells, labeled #1 and #2 (near
429 the west boundary), with injecting rates of 10.2, and 9.5 [L^3T^{-1}], respectively, and 3 pumping wells, labeled
430 #3, #4, and #5 (near the east boundary), with pumping rates of 5.7, 5.5 and 8.8 [L^3T^{-1}], respectively.
431 This setup induces a flow from left to right with the presence of three sinks which will act as attractors of
432 the contaminant plume. The initial piezometric heads are set to 8 [L].
433

434 There are also 25 observation wells (see Figure 3), which will be used during the updating step of the
435 restart NS-EnKF. The observation wells labeled #6, #7 and #8 will be used to display the performance
436 of the updated parameters in the forecast of piezometric heads and contaminant concentrations with the
437 final updated parameters. The number of observation wells could seem large; but, at this point, we wish to
438 test the feasibility of using the EnKF for the simultaneous source identification and conductivity estimation.
439 In practice, the density of observation wells may not be as large prior to contaminant detection; but, after
440 contamination has been detected, and if the solute is dangerous, the post-detection network could become
441 as dense, if not denser, as the one we have used.
442

443 Other parameters—which are considered as homogeneous for both aquifers—are: porosity of 0.3 [-],
444 longitudinal dispersivity of 0.2 [L], transverse to longitudinal dispersivity ratio of 0.01, no molecular diffusion,
445 and initial contaminant concentration of zero [ML^{-3}]. Considering the transport controlling parameters as
446 well as the initial conditions homogeneous, not subject to identification, and perfectly known makes the
447 experiment less realistic than we would like, but introducing the identification of the spatially variable
448 conductivity together with the contaminant source information is a big leap with respect to previous works
449

473 on this subject and brings us closer to a potential contamination identification in more realistic cases.

474
475
476
477 The total simulation time is 500 [T], discretized into 100 time steps of increasing size following a geometric
478 series with ratio 1.01. For this geometric series, the initial step is 2.93 [T]. Concentrations and piezometric
479 heads are observed during the first 60 time steps (for a total time of 239.5 [T]).

480
481 The release of the contaminant always starts at time 30 (around the 10th time step) and ends at time
482 100 (around the 30th time step). In the unimodal aquifer, the release is at location $(X, Y) = (11.5, 30.5)$ [L]
483 with a mass-loading rate of 100 [MT⁻¹]. We will refer to this case as scenario S1. In the channelized aquifer
484 we consider two different situations: in the first one, the release happens at location $(X, Y) = (11.5, 30.5)$
485 in a high permeability zone; and in the second one, the release happens at location $(X, Y) = (11.5, 19.5)$ in
486 a low permeability zone. The release load and timing is the same as for the other aquifer. We will refer to
487 these cases as scenarios S2 and S3, respectively. (Scenarios are summarized in Table 2.)

488
489 Two ensembles of 800 logconductivity realizations are generated, one for scenario S1 and another one for
490 scenarios S2 and S3. The random function models used for the generation of these ensembles are the same
491 as the ones used for the generation of the corresponding reference fields. They are unconditional realizations
492 based on their marginal distributions and the training image for S2 and S3.

493
494 Although in previous works we have shown that the impact of prior model selection is very limited [49, 50],
495 the knowledge of the marginal distribution of logconductivity could be considered as too advantageous.
496 For this reason, an additional scenario, referred to as S1b, is included in the Appendix. Scenario S1b is
497 a duplicate of scenario S1 but using a non-informative uniform marginal distribution for logconductivity
498 between $-1 [\ln(LT^{-1})]$ and $5 [\ln(LT^{-1})]$ for the generation of the initial ensemble of 800 realizations. This
499 scenario is not discussed within the main body of the paper. The reader is referred to the Appendix to
500 understand the impact that a non-informative prior has in the performance of the approach.

501
502 An ensemble of 800 7-tuplets for the source parameters is also generated, which will be used for the three
503 scenarios. Each member of this ensemble is attached to the realization with the same sequence order in
504 the initial ensemble of logconductivity fields. Employing 800 realizations in the ensemble helps in reducing
505 filter inbreeding and spurious correlations generally associated with small ensemble sizes [22, 23]. The
506 values of each 7-tuplet are generated, independently, from the following uniform distributions: initial release
507 time $T \in [10, 90]$, release duration $\Delta T \in [10, 110]$, mass-loading rate $M \in [50, 140]$, and source location
508 $(X, Y) \in [5, 15] \times [25, 35]$ for scenarios S1, and $(X, Y) \in [5, 15] \times [17, 35]$ for scenarios S2 and S3 (see Figure 1
509 for the areas of the prior guesses of the release locations). Notice that we have chosen intervals not centered
510 about the reference values, so that the means of the initial ensemble are biased with respect to the reference

532
533
534 values. Also notice that for the bimodal aquifer we initially allow that the source location be either in a low
535
536 or high permeability area.
537

538 539 **4. Results**

540
541 Figure 4 shows the contaminant plume evolution at the 10th (30.68 [T]), 30th (102.02 [T]), 40th (143.38
542 [T]), and 60th (239.53 [T]) time steps in the three reference scenarios. Figure 5 shows the evolution in time
543
544 of the total contaminant mass in the reference aquifers. Recall that the injection wells are near the western
545
546 boundary and pumping wells are near the eastern boundary, and that the contaminant release starts around
547
548 the 10th time step and stops around the 30th time step. The contaminant plume spreads from west to east
549
550 at different speeds and with different spreading rates depending on the scenario: in the unimodal aquifer
551
552 the solute travels more or less horizontally following the mean head gradient, and the plume does not reach
553
554 the pumping wells until about time 50; in the multimodal aquifer, the plume travels quickly in the high
555
556 conductivity zone and reaches the pumping wells at about the time the contaminant injections ceases, while
557
558 the plume moves very little in the low conductivity zone and has not reached the pumping wells at the end
559
560 of the simulation.

561
562 Figure 6 shows the ensemble mean and the ensemble variance of the updated log-conductivity fields after
563
564 the 60th time step for the three scenarios. Recall that there are no conditioning data used for the generation
565
566 of the initial log-conductivity fields, hence, the initial ensemble mean and initial ensemble variance are flat
567
568 and the values are equal to their prior global mean and variance. After observed piezometric head and
569
570 concentrations are assimilated, the ensemble mean of the updated log-conductivity fields can retrieve the
571
572 main patterns of the references. The ensemble variance of scenarios S1 gets close to zero for the most part
573
574 of the aquifer, whereas for scenario S2 and S3 the reduction is not as large, with still some uncertainties
575
576 corresponding with the boundaries of the channels. These results, which are consistent with previous findings
577
578 [23], indicate that the piezometric head information (the same for scenarios S2 and S3) is not enough
579
580 to fully identify the strong channels; concentration data also carries information about the conductivity
581
582 heterogeneity. In scenario S3 the plume has not traveled much and therefore the conductivity information
583
584 on the concentration data is smaller than for scenario S3 and, as a result, the ensemble variances are, overall,
585
586 larger than for S2.

587
588 Before the analysis of the results regarding the source parameters, we wish to analyze the reproduction of
589
590 the piezometric and concentration data at well locations #6, #7 and #8 (see Fig. 3) as well as of the spatial
591
592 distribution of piezometric head at the end of time step 60, and the spatiotemporal evolution of concentration.

591
592
593
594 236 Figures 7 and 8 show the evolution of piezometric heads and concentrations, respectively, at the three wells
595 237 as computed in each member of the initial ensemble for a simulation time of 500 (100 time steps), which goes
596 238 beyond the assimilation time of 240 (60 time steps). The initial realizations of conductivity are unconditional
597
598 239 and, consequently, the spread of the evolution of heads and concentrations through the ensemble is very large.
599
600 240 Figures 9 and 10 show the evolution of piezometric heads and concentrations, respectively, at the same three
601 241 wells, with the parameters updated after the 60th time step. We can observe that the reproduction of the
602 242 piezometric heads in the updated ensemble is almost perfect, while the reproduction of the concentrations
603
604 243 has improved considerably with respect to the predictions on the unconditional ensemble.

605
606 244 Figure 11 shows piezometric information at the end of time step 60. We have chosen to show the spatial
607 245 distribution of heads in the reference field, in a randomly selected realization (#29), the ensemble mean of
608 246 the 800 realizations and the ensemble variance. The good reproduction of the observed piezometric heads
609 247 at wells #6, #7 and #8, which were used in the assimilation steps, extends for the entire aquifer as it is
610 248 indicated by the almost zero variance in most of the aquifer for all scenarios, and by looking at the similarity
611 249 between the heads in the reference and the heads in a given realization or the ensemble mean. We have
612
613 250 chosen to show the results only for time step 60 and for a single realization because the results for other
614
615 251 time steps or other realizations are virtually the same.

616
617
618 252 A similar analysis is performed for concentrations. Figures 12, 13 and 14 show the time evolution of
619 253 concentration in three randomly selected realizations (#29, #537, and #695) for the three scenarios. When
620 254 looking at any of the columns in these figures we are observing the variability across realizations for different
621 255 time steps. While the plumes are similar, we can observe some differences for all scenarios and all time
622
623 256 steps; yet, the shapes and topologies of the plumes when compared to the reference ones in Figure 4 are well
624 257 reproduced. With the same observation wells for piezometric heads and concentrations, the reproduction
625
626 258 of the concentrations is harder to achieve since the reference plumes are only "seen" in a small number of
627
628 259 observation wells.

629
630 260 Notice also that each realization has associated a specific updated 7-tuple of contaminant source pa-
631 261 rameters, which explains why, for instance, the plume appears earlier in realization #29 than in the other
632
633 262 realizations because the starting time associated with that realization is smaller than 10.

634
635 263 The concentration time evolution derived from the updated realizations after 60 time steps of data
636 264 assimilation can be summarized by their ensemble mean and their ensemble variance displayed in Figures
637
638 265 15 and 16, respectively. As with the individual realizations, the mean map captures well the sizes and
639
640 266 topologies of the plumes in the reference, although it misses the reproduction of the maximum values.

650
651
652 The largest variances appear at the locations of the reference peak concentrations. We did not show the
653
654 corresponding maps computed with the initial ensemble of realizations, prior to any assimilation of data,
655
656 because in that case the mean plumes spread over the entire aquifer and the variances are very large. In our
657
658 examples, the ensemble Kalman filter shows again its potential to characterize the spatial heterogeneity of
659
660 hydraulic conductivity with the additional complication of not knowing, at the beginning of the simulation,
661
662 the time or the location of the contaminant source.

663 Finally, Figure 17 shows boxplots for the parameters that describe the contaminant source, i.e., $X, Y, T, \Delta T$
664
665 and M computed at different times during the assimilation process. Starting from an unknown spatial dis-
666
667 tribution of hydraulic conductivities and an unknown contaminant source, the use of a restart NS-EnKF
668
669 and the assimilation of piezometric heads and solute concentrations from a network of observation wells, we
670
671 end with a reasonable characterization of the spatial variability of hydraulic conductivities (independently
672
673 of whether the underlying reference follows a Gaussian —unimodal— distribution or not) and a reasonable
674
675 identification of when, where and how much solute entered in the aquifer. Characterization that is duly
676
677 quantified with an uncertainty derived from the analysis of the ensemble of realizations. Regarding the
678
679 parameters describing the source, we can see that for almost all of them, at time step 60, the median values
680
681 (red bars in the boxplots) are quite close to the reference ones. The exceptions are the initial time for S3
682
683 (release in the channeled aquifer in a low conductivity zone) and the mass-loading rate for S1 (release in
684
685 the unimodal aquifer). The result for the initial time in S3 can only be interpreted in view of the overall
686
687 uncertainties of all source parameters for this scenario; while they have reduced with respect to their initial
688
689 uncertainties at time zero, the reduction is not very large for many of them, and this is due to the little
690
691 concentration information collected (refer to Figure 4, third row, to see the evolution of the plume in the
692
693 reference field with respect to the observation locations), therefore the conclusion is that more concentration
694
695 data would be needed for a better characterization of the source parameters in S3. In the cases of S1, the
696
697 median values of all parameters converge very quickly to the reference values and after time step 30 they do
698
699 not change much except for the mass loading, for which the median value keeps increasing as time passes
700
701 and the remaining uncertainty is still large. The mass loading is, for all scenarios, the parameter that con-
702
703 sistently gets the larger uncertainty at the end of the assimilation period for all parameters and this must
704
705 be attributed to the dilution of the plume concentration, which makes that the absolute differences between
706
707 the observed concentrations at the wells and the predicted values are small even for relatively large changes
708
709 in the mass loading at the injection point.

709 Each scenario behaves differently regarding the identification of the source parameters. In S1, the median

709
710
711
712 298 value for the X coordinate is close to the reference one, but the uncertainty is large; this large uncertainty in
713 299 X could be explained by the same reason as the large uncertainty in the mass-loading rate: the dilution of
714 300 the plume together with its longitudinal spreading makes that changes in X do not introduce large absolute
715 301 changes of concentrations at the observation locations. The contrary happens with Y , its median value
716 302 converges almost exactly to the reference value at time step 30 and remains there for the rest of the simulation;
717 303 considering that transversal dispersivity is small, changes in Y will introduce noticeable modifications in the
720 304 concentrations at observation wells, making it a more sensitive parameter for identification purposes. The
722 305 median starting time T and the median injection time ΔT converge also quickly to the reference values,
723 306 with residual uncertainties considerably smaller than their starting ones. In S2, the identification of Y , T
724 307 and ΔT by their median values is remarkable, with very little uncertainty left; the value of X is also well
726 308 identified but with larger uncertainty than the previous parameters; again, the explanation could be the
728 309 same as for S1, a small sensitivity of concentrations to fluctuations of X about its reference value. The
729 310 mass-loading rate is correctly identified by its median value, and the interquartile range is one third of its
730 311 value at the beginning of the simulation, yet, with regard to the other parameters its uncertainty is still
732 312 large; the explanation for this large uncertainty is again related to the small sensitivity of the concentrations
733 313 at the observation locations to changes of the mass loading within its uncertainty interval. Finally, in S3,
734 314 as it was already pointed out, the plume displaces very little during the 60 time steps and the amount of
735 315 information carried by the solute concentrations at the observation locations is small; yet, the algorithm
736 316 is able to identify the source coordinates X and Y by their median values, and their final uncertainty is
737 317 not very large. Notice that for S3, contrary to S2, displacing vertically the release location does not have
738 318 such a large impact in the plume movement for the duration of the assimilation period, therefore, the final
739 319 uncertainty is larger than for S2. The release duration ends also with a large uncertainty, but this is due to
740 320 the large uncertainty associated to the release initial time, and the mass-loading rate also ends with a large
741 321 uncertainty for the same reasons discussed above for S1 and S2.

748 749 750 322 **5. Summary and conclusions**

751
752 323 In this work, we have removed one of the most critical limitations of our previous work [21], in which we
753 324 demonstrated the application of the restart NS-EnKF for contaminant source identification but assuming
754 325 that the spatial heterogeneity of hydraulic conductivities was perfectly known. The joint identification of
755 326 hydraulic conductivities and contaminant source information has been performed for three different scenarios
756 327 combining unimodal and bimodal conductivity distributions (with and without channeling) and releases in
757
758
759
760
761
762
763
764
765
766
767

768
769
770 high and low conductivity zones. The results show that such an identification is possible but that the uncer-
771
772 tainty associated with the final ensembles of realizations is still significant, especially regarding concentration
773
774 spatiotemporal evolution and some of the parameters identifying the source.

775 The analysis was performed assuming that no information on conductivities is available except for their
776
777 marginal distributions. (An additional scenario in which the marginal distribution is also unknown is included
778
779 in the appendix showing the small impact that this knowledge has in the final results.) In practice, there are
780
781 always some measurements of conductivity, which, if included as conditioning data, would help in improving
782
783 the overall characterization as already shown elsewhere [23]. The analysis was also performed assuming that
784
785 initial and boundary conditions are perfectly known, and that the transport parameters, such as porosity
786
787 or dispersivity, are also perfectly known. In practice this will never be the case, and either they should be
788
789 included in the identification process or they should be modeled accounting for their uncertainty.

787 The final uncertainties on the conductivity spatial distribution and on the contaminant source parameters
788
789 should not be considered as a failure of the method to solve the problem but as a measure of the information
790
791 content of the available observations. Careful analysis of these uncertainties should be used to guide a
792
793 possible redesign of the sampling network.

793 In summary, we believe that the restart normal-score ensemble Kalman filter has the potential of helping
794
795 in the joint identification of a contaminant source and the spatial heterogeneity of conductivity, and that we
796
797 have advanced substantially from previous works in which the spatial heterogeneity of conductivity was not
798
799 considered.

800
801 **Acknowledgements** Financial support to carry out this work was received from the Spanish Ministry of
802
803 Economy and Competitiveness through project CGL2014-59841-P. The authors acknowledge the Associate
804
805 Editor, and the anonymous reviewers for their thoughtful and constructive comments.

806 807 **Appendix. Non-informative prior marginal distribution**

808
809 All scenarios in the main body of the paper have been generated assuming that the marginal distribution of
810
811 the logconductivities is known. However, in reality, this will not be so and there always be some uncertainty
812
813 about this distribution. To evaluate the impact of this uncertainty we have run an additional scenario,
814
815 which we refer as S1b, as a duplicate of scenario S1 but using a non-informative prior marginal distribution
816
817 of logconductivity: a uniform distribution between $-1 [\ln(LT^{-1})]$ and $5 [\ln(LT^{-1})]$. Such an analysis in the
818
819 context of just logconductivity identification has already been performed by us in the past [49, 50] showing

827
828
829 357 that the prior model selection has little impact in the performance of the NS-EnKF. A conclusion that
830 358 could be already anticipated by looking at the figures associated with the initial ensemble of unconditional
831 359 realizations in the main body of the paper.

834 360 Except for the marginal distribution used for the generation of the initial ensemble of realizations, all
835 361 remaining parameters and the different steps of the analysis are exactly the same as for S1. Next, we show
836 362 the same sets of figures as shown for scenario S1 in the body of the paper: in Figure 18 the ensemble mean
837 363 and ensemble variance of the updated $\ln K$, in Figure 19 the time evolution of the piezometric heads and
838 364 concentrations at three well locations #6, #7 and #8 for the initial ensemble of parameters, in Figure 20
839 365 the time evolution of the piezometric heads and concentrations at the same three well locations for the
840 366 parameters updated after the 60th time step, in Figure 21 the piezometric heads at the end of the 60th time
841 367 step, in Figure 22 the evolution of the contaminant plume in the 29th, 537th, and 695th realizations with
842 368 the parameters updated after the 60th time step in Figure 23 the ensemble mean and ensemble variance of
843 369 the contaminant plume evolution with the parameters updated after the 60th time step, and in 24 the box
844 370 plots of the source parameters.

851 371 A quick comparison of any of these figures with the corresponding ones for S1 shows small changes with
852 372 a final performance of S1b very similar to S1. The final updated parameters are virtually the same in S1b
853 373 and S1. The variance of the updated logconductivities is slightly larger towards the edge of the fields for
854 374 S1b than for S1. The predicted piezometric heads and concentrations on the updated fields are almost the
855 375 same in S1 and S1b. And the boxplots for the contaminant source parameters are also very similar when
856 376 comparing S1 and S1b.

860 377 In summary, the NS-EnKF is capable to update an ensemble of initial realizations with a prior distri-
861 378 bution probability far from the true one into an ensemble of realizations that will be conditioned to the
862 379 observation data and converge towards the reproduction of the reference logconductivity field as well as
863 380 capture the parameters defining the unknown contamination source. These results are in line of previous
864 381 analysis of the NS-EnKF that proved its updating power of an initial ensemble of realizations even when
865 382 these initial ensemble is far from the reference field due to lack of information about the spatial variability
866 383 of logconductivity [49, 50].

871 384 [1] Gorelick, S.M., Evans, B., Remson, I. Identifying sources of groundwater pollution: an optimization
872 385 approach. *Water Resources Research* 1983;19(3):779–790.

875 386 [2] Sun, A.Y., Painter, S.L., Wittmeyer, G.W.. A constrained robust least squares approach for contam-

- 886
887
888
889 387 inant release history identification. *Water resources research* 2006;42(4).
- 890
891 388 [3] Sun, A.Y., Painter, S.L., Wittmeyer, G.W.. A robust approach for iterative contaminant source
892 389 location and release history recovery. *Journal of contaminant hydrology* 2006;88(3):181–196.
- 893
894 390 [4] Aral, M.M., Guan, J., Maslia, M.L.. Identification of contaminant source location and release history
895 391 in aquifers. *Journal of hydrologic engineering* 2001;6(3):225–234.
- 896
897
898 392 [5] Yeh, H.D., Chang, T.H., Lin, Y.C.. Groundwater contaminant source identification by a hybrid
899 393 heuristic approach. *Water Resources Research* 2007;43(9).
- 900
901 394 [6] Yeh, H.D., Lin, C.C., Yang, B.J.. Applying hybrid heuristic approach to identify contaminant source
902 395 information in transient groundwater flow systems. *Mathematical Problems in Engineering* 2014;2014.
- 903
904
905 396 [7] Mirghani, B.Y., Mahinthakumar, K.G., Tryby, M.E., Ranjithan, R.S., Zechman, E.M.. A parallel
906 397 evolutionary strategy based simulation–optimization approach for solving groundwater source identifi-
907 398 cation problems. *Advances in Water Resources* 2009;32(9):1373–1385.
- 909
910 399 [8] Dokou, Z., Pinder, G.F.. Optimal search strategy for the definition of a dnapl source. *Journal of*
911 400 *Hydrology* 2009;376(3):542–556.
- 912
913
914 401 [9] Amirabdollahian, M., Datta, B.. Identification of pollutant source characteristics under uncertainty
915 402 in contaminated water resources systems using adaptive simulated anealing and fuzzy logic. *Int J of*
916 403 *GEOMATE* 2014;6(1):757–762.
- 917
918
919 404 [10] Ayvaz, M.T.. A hybrid simulation–optimization approach for solving the areal groundwater pollution
920 405 source identification problems. *Journal of Hydrology* 2016;538:161–176.
- 921
922
923 406 [11] Butera, I., Tanda, M.G., Zanini, A.. Simultaneous identification of the pollutant release history and
924 407 the source location in groundwater by means of a geostatistical approach. *Stochastic Environmental*
925 408 *Research and Risk Assessment* 2013;27(5):1269–1280.
- 926
927
928 409 [12] Cupola, F., Tanda, M.G., Zanini, A.. Laboratory sandbox validation of pollutant source location
929 410 methods. *Stochastic Environmental Research and Risk Assessment* 2015;29(1):169–182.
- 930
931
932 411 [13] Gzyl, G., Zanini, A., Fraczek, R., Kura, K.. Contaminant source and release history identification
933 412 in groundwater: A multi-step approach. *Journal of contaminant hydrology* 2014;157:59–72.
- 934
935
936
937
938
939
940
941
942
943
944

- 945
946
947
948 [14] Wagner, B.J.. Simultaneous parameter estimation and contaminant source characterization for coupled
949 413 groundwater flow and contaminant transport modelling. *Journal of Hydrology* 1992;135(1):275–303.
950
951 [15] Sidauruk, P., Cheng, A.D., Ouazar, D.. Ground water contaminant source and transport parameter
952 414 identification by correlation coefficient optimization. *Ground Water* 1998;36(2):208–214.
953
954 [16] Mahar, P.S., Datta, B.. Identification of pollution sources in transient groundwater systems. *Water*
955 417 *Resources Management* 2000;14(3):209–227.
956
957 [17] Mahar, P.S., Datta, B.. Optimal identification of ground-water pollution sources and parameter
958 419 estimation. *Journal of Water Resources Planning and Management* 2001;127(1):20–29.
959
960 [18] Singh, R.M., Datta, B.. Groundwater pollution source identification and simultaneous parameter
961 421 estimation using pattern matching by artificial neural network. *Environmental Forensics* 2004;5(3):143–
962 422 153.
963
964 [19] Datta, B., Chakrabarty, D., Dhar, A.. Simultaneous identification of unknown groundwater pollution
965 423 sources and estimation of aquifer parameters. *Journal of Hydrology* 2009;376(1):48–57.
966
967 [20] Koch, J., Nowak, W.. Identification of contaminant source architectures a statistical inversion that
968 424 emulates multiphase physics in a computationally practicable manner. *Water Resources Research*
969 425 2016;52(2):1009–1025.
970
971 [21] Xu, T., Gómez-Hernández, J.J.. Joint identification of contaminant source location, initial release
972 426 time, and initial solute concentration in an aquifer via ensemble kalman filtering. *Water Resources*
973 427 *Research* 2016;52(8):6587–6595.
974
975 [22] Hendricks Franssen, H.J., Kinzelbach, W.. Ensemble kalman filtering versus sequential self-calibration
976 429 for inverse modelling of dynamic groundwater flow systems. *Journal of Hydrology* 2009;365(3-4):261–
977 430 274.
978
979 [23] Xu, T., Gómez-Hernández, J.J., Zhou, H., Li, L.. The power of transient piezometric head data
980 431 in inverse modeling: an application of the localized normal-score enkf with covariance inflation in a
981 432 heterogenous bimodal hydraulic conductivity field. *Advances in Water Resources* 2013;54:100–118.
982
983 [24] Xu, T., Gómez-Hernández, J.J.. Probability fields revisited in the context of ensemble kalman filtering.
984 433
985 434
986
987
988
989
990
991
992
993
994
995
996
997
998
999
1000
1001
1002
1003

- 1004
1005
1006
1007 440 [25] Schöniger, A., Nowak, W., Franssen, H.. Parameter estimation by ensemble kalman filters with
1008 441 transformed data: Approach and application to hydraulic tomography. *Water Resources Research*
1009 442 2012;48(4):W04502.
- 1010
1011
1012 443 [26] Gómez-Hernández, J.J., Wen, X.H.. Probabilistic assessment of travel times in groundwater modeling.
1013 444 *Stochastic Hydrology and Hydraulics* 1994;8(1):19–55.
- 1014
1015
1016 445 [27] Troldborg, M., Nowak, W., Tuxen, N., Bjerg, P.L., Helmig, R., Binning, P.J.. Uncertainty evaluation
1017 446 of mass discharge estimates from a contaminated site using a fully bayesian framework. *Water Resources*
1018 447 *Research* 2010;46(12).
- 1019
1020
1021 448 [28] Evensen, G.. Sequential data assimilation with a nonlinear quasi-geostrophic model using monte carlo
1022 449 methods to forecast error statistics. *J Geophys Res* 1994;99(10):143–10.
- 1023
1024 450 [29] Simon, E., Bertino, L.. Gaussian anamorphosis extension of the denkf for combined state parameter
1025 451 estimation: Application to a 1d ocean ecosystem model. *Journal of Marine Systems* 2012;89(1):1–18.
- 1026
1027
1028 452 [30] Burgers, G., van Leeuwen, P., Evensen, G., Instituut, K.N.M.. Analysis scheme in the ensemble
1029 453 kalman filter. *Monthly weather review* 1998;126(6):1719–1724.
- 1030
1031 454 [31] Wen, X., Chen, W.. Real-time reservoir model updating using ensemble kalman filter with confirming
1032 455 option. *SPE Journal* 2006;11(4):431–442.
- 1033
1034
1035 456 [32] Chen, Y., Zhang, D.. Data assimilation for transient flow in geologic formations via ensemble kalman
1036 457 filter. *Advances in Water Resources* 2006;29(8):1107–1122.
- 1037
1038
1039 458 [33] Xu, T., Gómez-Hernández, J.J., Li, L., Zhou, H.. Parallelized ensemble kalman filter for hydraulic
1040 459 conductivity characterization. *Computers & Geosciences* 2013;52:42–49.
- 1041
1042
1043 460 [34] Camporese, M., Cassiani, G., Deiana, R., Salandin, P.. Assessment of local hydraulic properties from
1044 461 electrical resistivity tomography monitoring of a three-dimensional synthetic tracer test experiment.
1045 462 *Water Resources Research* 2011;47(12).
- 1046
1047
1048 463 [35] Camporese, M., Cassiani, G., Deiana, R., Salandin, P., Binley, A.. Coupled and uncoupled
1049 464 hydrogeophysical inversions using ensemble kalman filter assimilation of ert-monitored tracer test data.
1050 465 *Water Resources Research* 2015;51(5):3277–3291.

- 1063
1064
1065
1066 466 [36] Crestani, E., Campoprese, M., Baú, D., Salandin, P. Ensemble kalman filter versus ensemble
1067 467 smoother for assessing hydraulic conductivity via tracer test data assimilation. *Hydrology and Earth*
1068 System Sciences 2013;17(4):1517.
1069 468
- 1070 469 [37] Crestani, E., Campoprese, M., Salandin, P. Assessment of hydraulic conductivity distributions
1071 470 through assimilation of travel time data from ert-monitored tracer tests. *Advances in Water Resources*
1072 471 2015;84:23–36.
- 1073 472 [38] Bear, J.. *Dynamics of fluids in porous media*. New York, 764pp: American Elsevier Pub. Co.; 1972.
1074 473 ISBN 9780444001146.
- 1075 474 [39] Zheng, C.. *Mt3dms v5. 3supplemental users guide*: Tuscaloosa, ala., university of alabama department
1076 475 of geological sciences. Tech. Rep.; Technical Report to the US Army Engineer Research and Development
1077 476 Center; 2010.
- 1078 477 [40] McDonald, M., Harbaugh, A.. *A modular three-dimensional finite-difference ground-water flow model*
1079 478 1988;.
- 1080 479 [41] Ma, R., Zheng, C., Zachara, J.M., Tonkin, M.. Utility of bromide and heat tracers for aquifer
1081 480 characterization affected by highly transient flow conditions. *Water Resources Research* 2012;48(8).
- 1082 481 [42] Apte, A., Hairer, M., Stuart, A., Voss, J.. Sampling the posterior: An approach to non-gaussian
1083 482 data assimilation. *Physica D: Nonlinear Phenomena* 2007;230(1):50–64.
- 1084 483 [43] Chen, Y., Oliver, D.S., et al. Parameterization techniques to improve mass conservation and data as-
1085 484 similation for ensemble kalman filter. In: *SPE western regional meeting*. Society of Petroleum Engineers;
1086 485 2010;.
- 1087 486 [44] Zhou, H., Gómez-Hernández, J.J., Hendricks Franssen, H., Li, L.. An approach to handling non-
1088 487 gaussianity of parameters and state variables in ensemble kalman filtering. *Advances in Water Resources*
1089 488 2011;34(7):844–864.
- 1090 489 [45] Sun, A., Morris, A., Mohanty, S.. Sequential updating of multimodal hydrogeologic parameter fields
1091 490 using localization and clustering techniques. *Water Resources Research* 2009;45(7):W07424.
- 1092 491 [46] Simon, E., Bertino, L.. Application of the gaussian anamorphosis to assimilation in a 3-d cou-
1093 492 pled physical-ecosystem model of the north atlantic with the enkf: a twin experiment. *Ocean Science*
1094 493 2009;5(4):495–510.

1122
1123
1124
1125 494 [47] Gómez-Hernández, J.J., Journel, A.G.. Joint sequential simulation of multi-Gaussian fields. *Geostatistics Troia* 1993;92(1):85–94.
1126 495
1127
1128 496 [48] Strebelle, S.. Conditional simulation of complex geological structures using multiple-point statistics.
1129 497 *Mathematical Geology* 2002;34(1):1–21.
1130
1131
1132 498 [49] Li, L., Zhou, H., Hendricks Franssen, H., Gómez-Hernández, J.J.. Groundwater flow inverse mod-
1133 499 eling in non-multigaussian media: performance assessment of the normal-score ensemble kalman filter.
1134 500 *Hydrology and Earth System Sciences* 2012;16(2):573.
1135
1136
1137 501 [50] Zhou, H., Li, L., Gómez-Hernández, J.J.. Characterizing curvilinear features using the localized
1138 502 normal-score ensemble kalman filter. In: *Abstract and Applied Analysis*; vol. 2012. Hindawi Publishing
1139 503 Corporation; 2012,.
1140
1141
1142
1143
1144
1145
1146
1147
1148
1149
1150
1151
1152
1153
1154
1155
1156
1157
1158
1159
1160
1161
1162
1163
1164
1165
1166
1167
1168
1169
1170
1171
1172
1173
1174
1175
1176
1177
1178
1179
1180

Table 1: Parameters of the random functions describing the heterogeneity of $\ln K$ for the two aquifers. λ_x and λ_y are the ranges in the x and y directions of an exponential covariance.

$\ln K$	Facies	Proportion	Mean	Std. dev	Variogram type	λ_x	λ_y	sill
Unimodal aquifer			2.0	1.5	exponential	20	20	1
Channelized aquifer	Channel	0.35	1.0	1.0	exponential	20	20	1
	Non-channel	0.65	-2.5	0.6	exponential	20	20	0.35

Table 2: Definition of scenarios.

Scenario	S1	S2	S3
Unimodal aquifer	✓		
Channelized aquifer		✓	✓
Source location (11.5, 30.5)	✓	✓	
Source location (11.5, 19.5)			✓

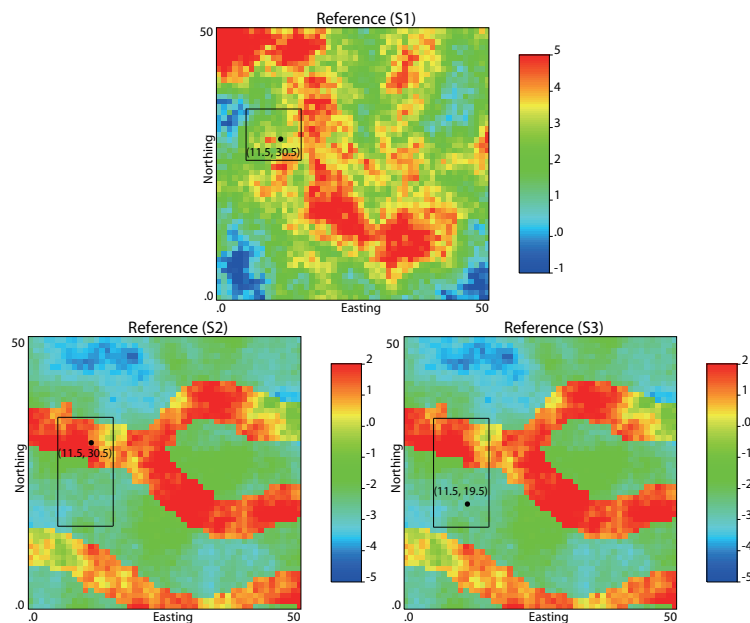


Figure 1: Scenarios S1-S3. Reference fields of $\ln K$. The black circle denotes the source location. The black quadrilateral is the suspect area to be used in the identification step.

1240
1241
1242
1243
1244
1245
1246
1247
1248
1249
1250
1251
1252
1253
1254
1255
1256
1257
1258
1259
1260
1261
1262
1263
1264
1265
1266
1267
1268
1269
1270
1271
1272
1273
1274
1275
1276
1277
1278
1279
1280
1281
1282
1283
1284
1285
1286
1287
1288
1289
1290
1291
1292
1293
1294
1295
1296
1297
1298

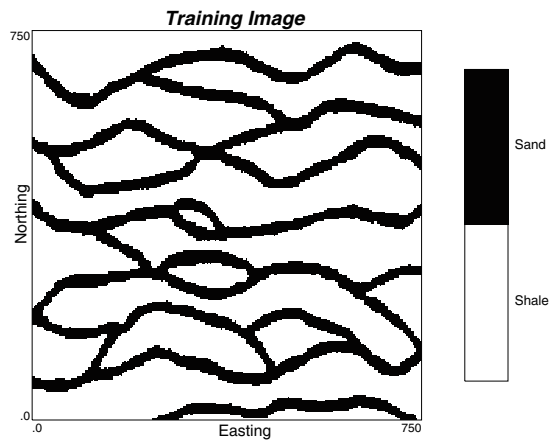


Figure 2: Training image.

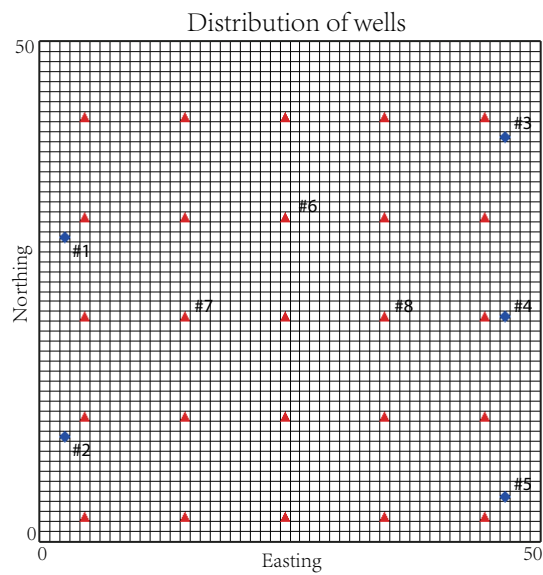


Figure 3: Distribution of wells. Red triangles are measurement wells; blue diamonds are injection wells near the west boundary and pumping wells near the east boundary.

1299
 1300
 1301
 1302
 1303
 1304
 1305
 1306
 1307
 1308
 1309
 1310
 1311
 1312
 1313
 1314
 1315
 1316
 1317
 1318
 1319
 1320
 1321
 1322
 1323
 1324
 1325
 1326
 1327
 1328
 1329
 1330
 1331
 1332
 1333
 1334
 1335
 1336
 1337
 1338
 1339
 1340
 1341
 1342
 1343
 1344
 1345
 1346
 1347
 1348
 1349
 1350
 1351
 1352
 1353
 1354
 1355
 1356
 1357

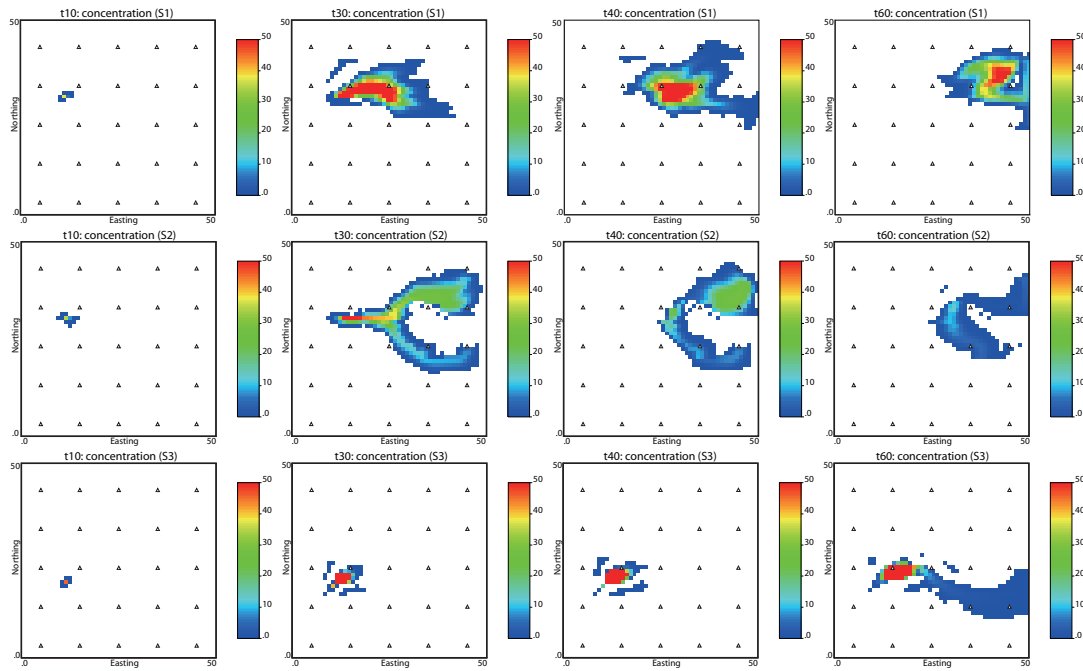


Figure 4: Scenarios S1-S3. Contaminant plume evolution at the 10th (beginning of solute injection), 30th (end of solute injection), 40th and 60th time steps in the reference aquifers. White triangles mark the measurement wells.

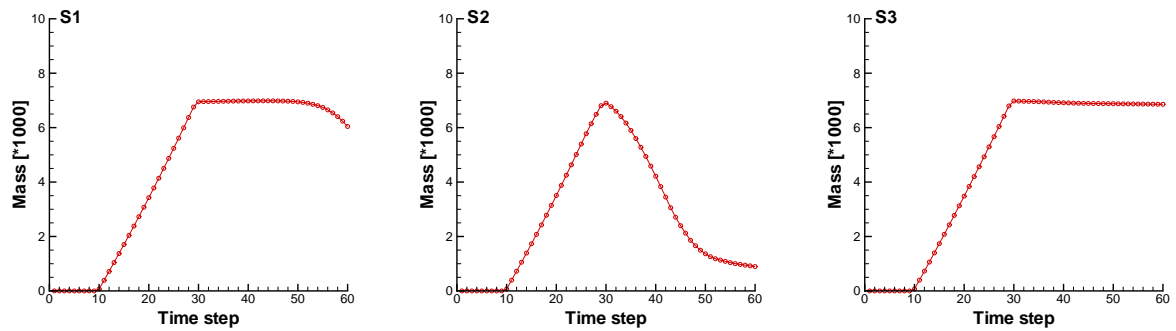


Figure 5: Scenarios S1-S3. Time evolution of the total solute mass in the aquifer.

1358
 1359
 1360
 1361
 1362
 1363
 1364
 1365
 1366
 1367
 1368
 1369
 1370
 1371
 1372
 1373
 1374
 1375
 1376
 1377
 1378
 1379
 1380
 1381
 1382
 1383
 1384
 1385
 1386
 1387
 1388
 1389
 1390
 1391
 1392
 1393
 1394
 1395
 1396
 1397
 1398
 1399
 1400
 1401
 1402
 1403
 1404
 1405
 1406
 1407
 1408
 1409
 1410
 1411
 1412
 1413
 1414
 1415
 1416

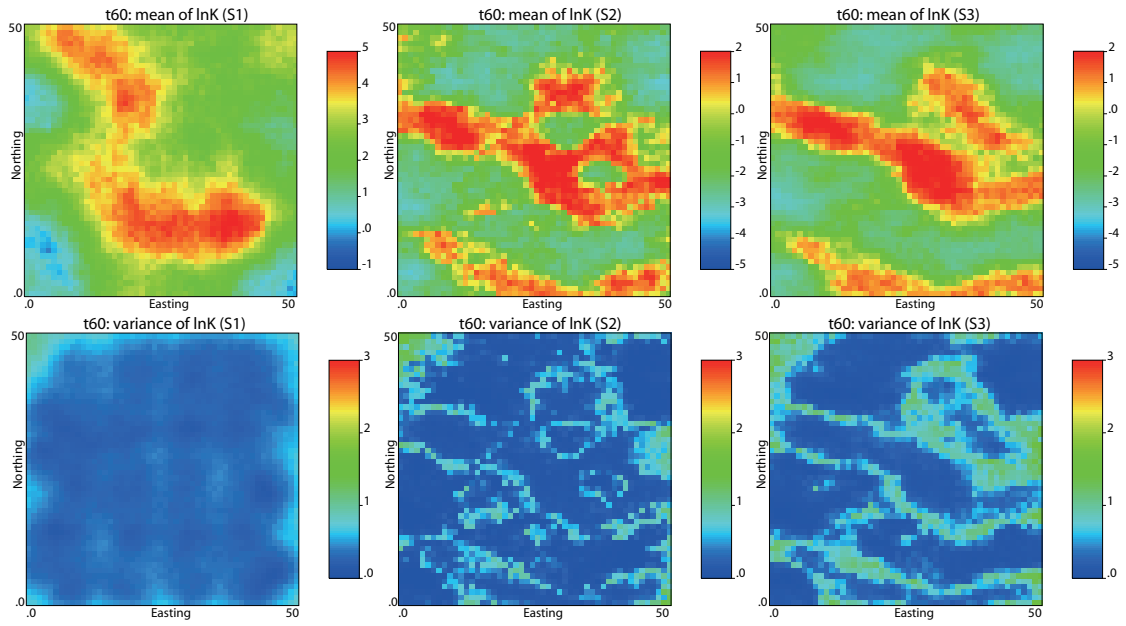


Figure 6: Scenarios S1-S3. Updated ensemble mean (top row) and updated ensemble variance (bottom row) of $\ln K$ after the 60th time step.

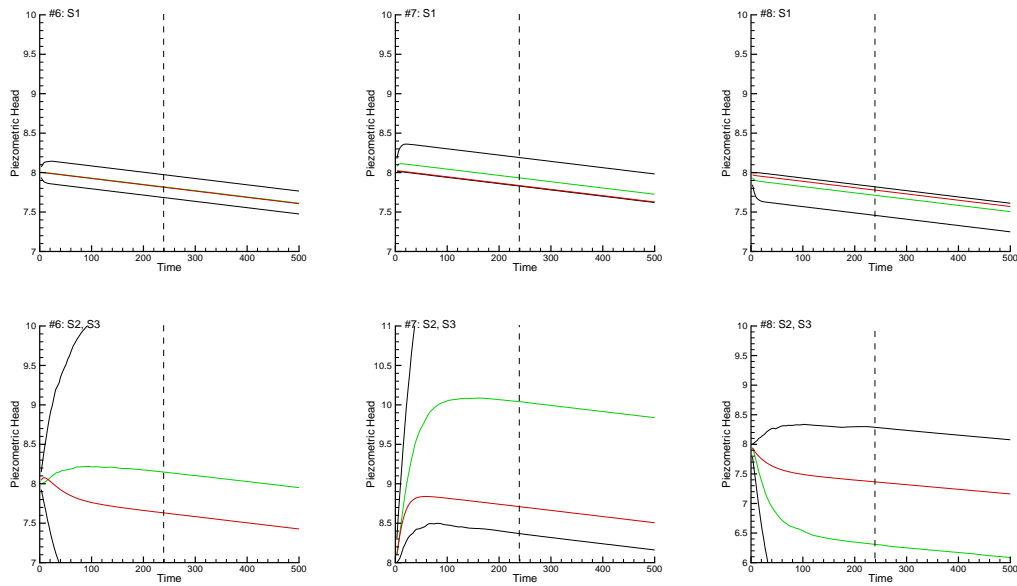


Figure 7: Scenarios S1-S3. Time evolution of the piezometric heads at the three wells #6, #7 and #8 for the initial ensemble of source information parameters and $\ln K$. The red line is the evolution of the piezometric head in the reference. The black lines correspond to the 5 and 95 percentiles of all realizations, and the green line corresponds to the median. The vertical dashed lines mark the end of the assimilation period.

1417
1418
1419
1420
1421
1422
1423
1424
1425
1426
1427
1428
1429
1430
1431
1432
1433
1434
1435
1436
1437
1438
1439
1440
1441
1442
1443
1444
1445
1446
1447
1448
1449
1450
1451
1452
1453
1454
1455
1456
1457
1458
1459
1460
1461
1462
1463
1464
1465
1466
1467
1468
1469
1470
1471
1472
1473
1474
1475

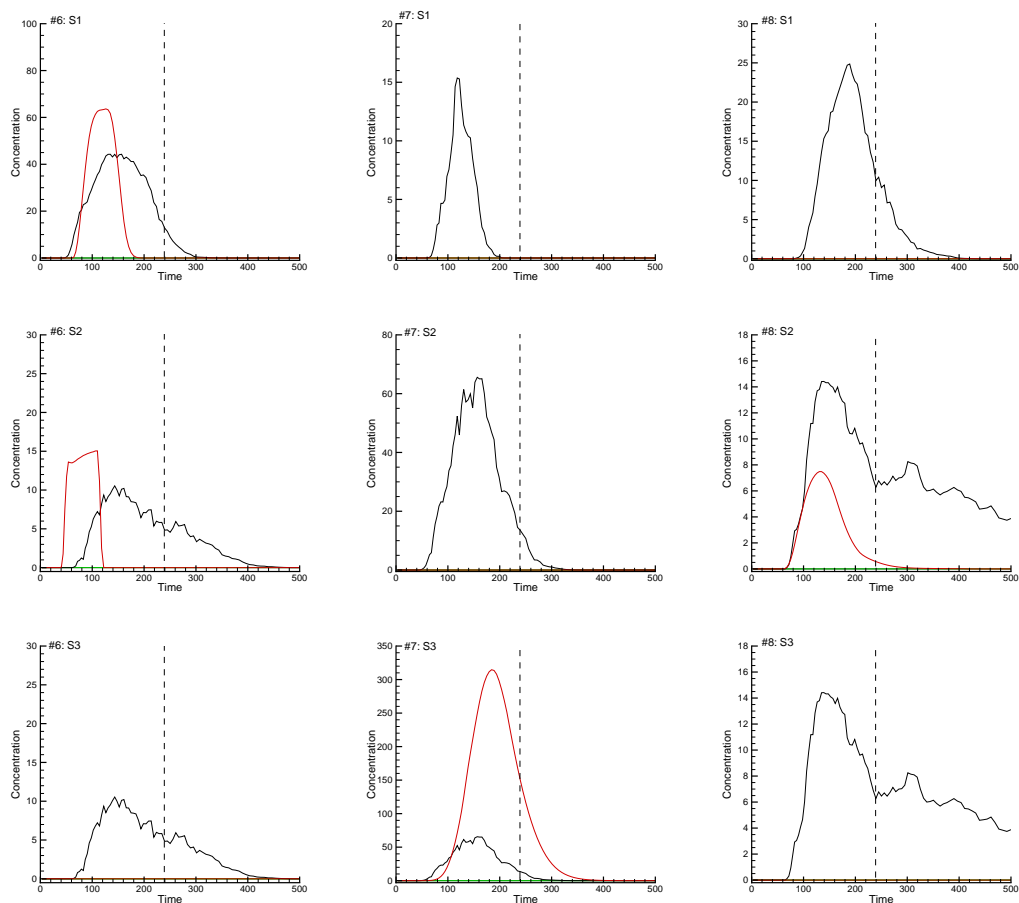


Figure 8: Scenarios S1-S3. Same caption as previous figure but regarding solute concentration.

1476
1477
1478
1479
1480
1481
1482
1483
1484
1485
1486
1487
1488
1489
1490
1491
1492
1493
1494
1495
1496
1497
1498
1499
1500
1501
1502
1503
1504
1505
1506
1507
1508
1509
1510
1511
1512
1513
1514
1515
1516
1517
1518
1519
1520
1521
1522
1523
1524
1525
1526
1527
1528
1529
1530
1531
1532
1533
1534

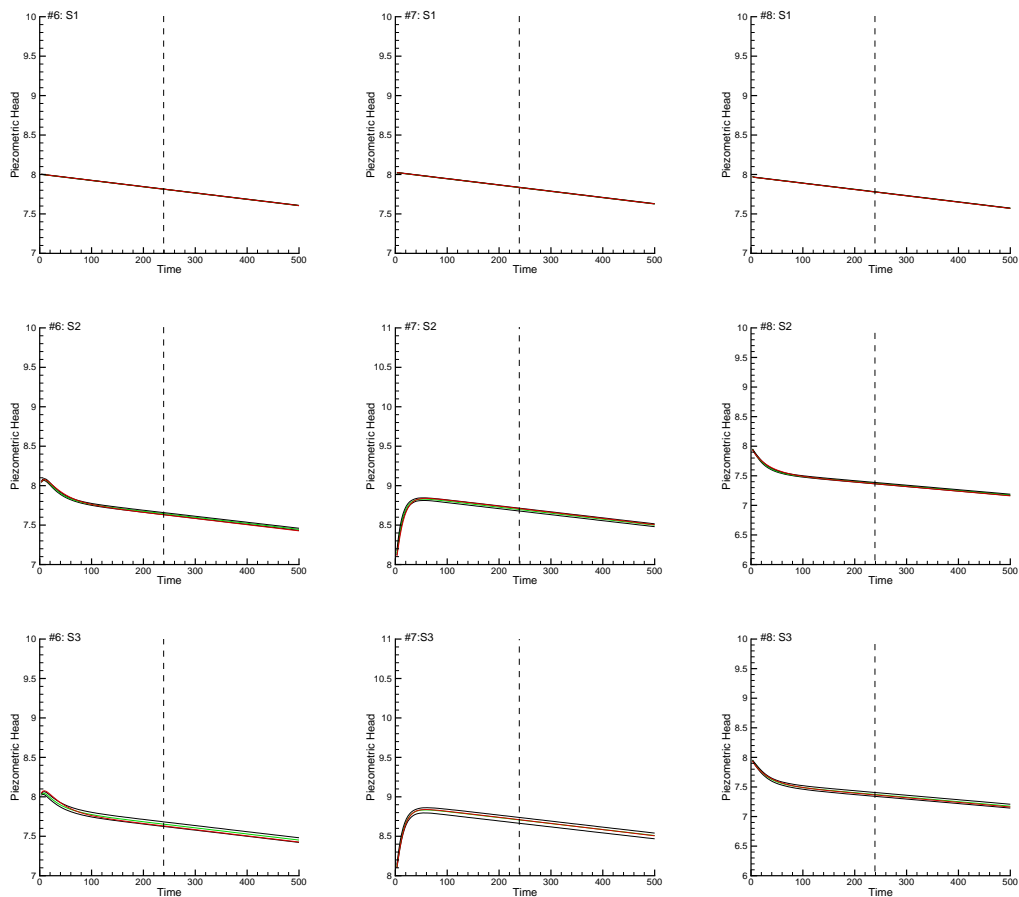


Figure 9: Scenarios S1-S3. Same caption as previous figure but regarding piezometric heads computed on the updated ensembles after the 60th assimilation time step.

1535
1536
1537
1538
1539
1540
1541
1542
1543
1544
1545
1546
1547
1548
1549
1550
1551
1552
1553
1554
1555
1556
1557
1558
1559
1560
1561
1562
1563
1564
1565
1566
1567
1568
1569
1570
1571
1572
1573
1574
1575
1576
1577
1578
1579
1580
1581
1582
1583
1584
1585
1586
1587
1588
1589
1590
1591
1592
1593

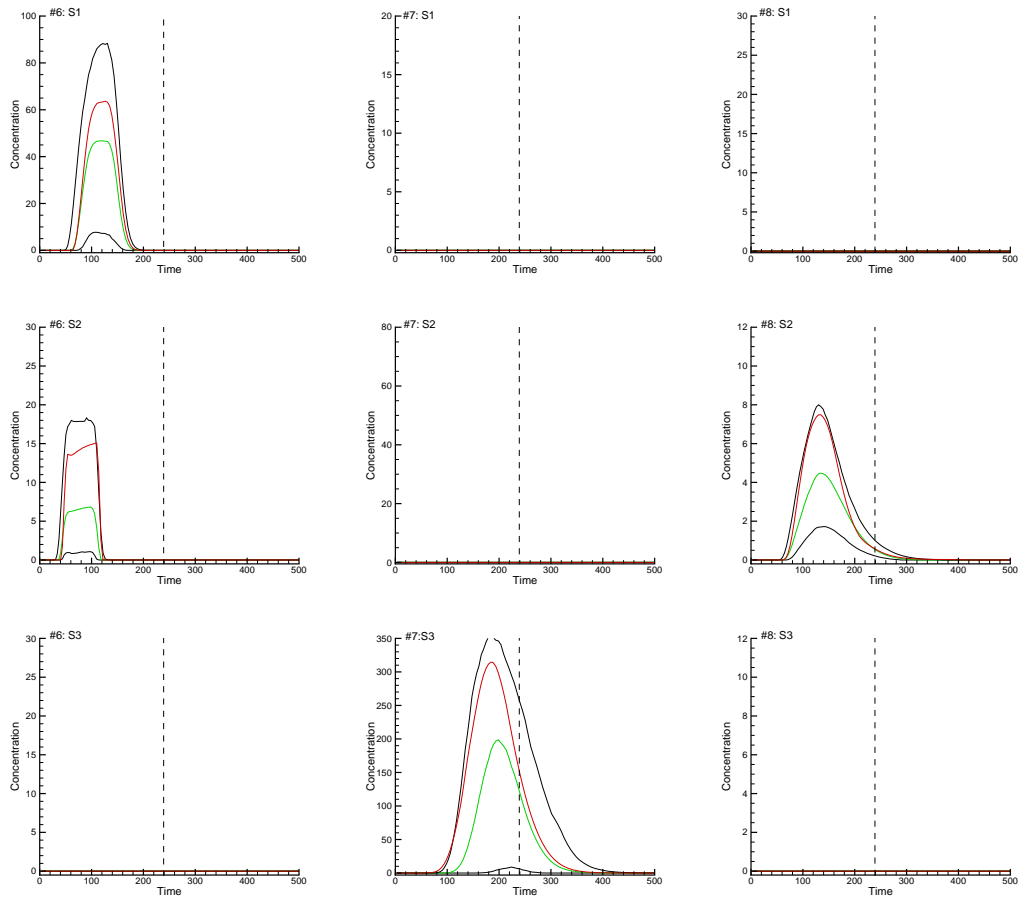


Figure 10: Scenarios S1-S3. Same caption as previous figure but regarding solute concentrations computed on the updated ensembles after the 60th assimilation time step

1594
1595
1596
1597
1598
1599
1600
1601
1602
1603
1604
1605
1606
1607
1608
1609
1610
1611
1612
1613
1614
1615
1616
1617
1618
1619
1620
1621
1622
1623
1624
1625
1626
1627
1628
1629
1630
1631
1632
1633
1634
1635
1636
1637
1638
1639
1640
1641
1642
1643
1644
1645
1646
1647
1648
1649
1650
1651
1652

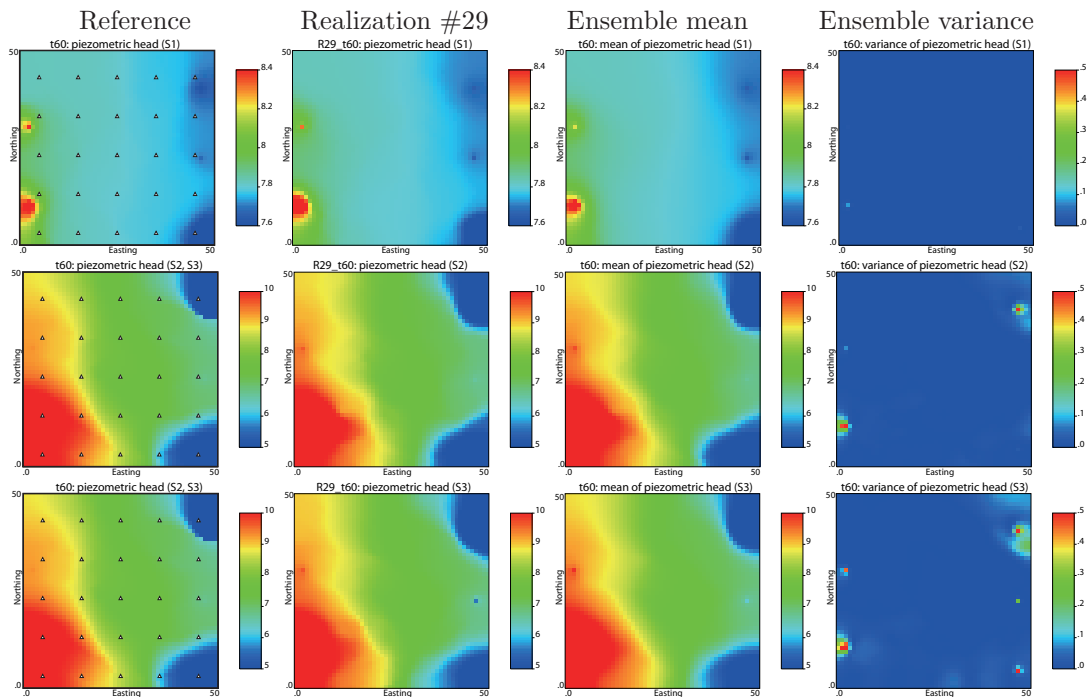


Figure 11: Piezometric heads at the end of the 60th time step for the three scenarios. From top to bottom, scenarios S1, S2 and S3. From left to right, heads in the reference aquifer; heads in realization #29; ensemble mean, and ensemble variance. White triangles mark the measurement wells. Note that the scale bar for S1 is different from that for S2 and S3.

1653
1654
1655
1656
1657
1658
1659
1660
1661
1662
1663
1664
1665
1666
1667
1668
1669
1670
1671
1672
1673
1674
1675
1676
1677
1678
1679
1680
1681
1682
1683
1684
1685
1686
1687
1688
1689
1690
1691
1692
1693
1694
1695
1696
1697
1698
1699
1700
1701
1702
1703
1704
1705
1706
1707
1708
1709
1710
1711

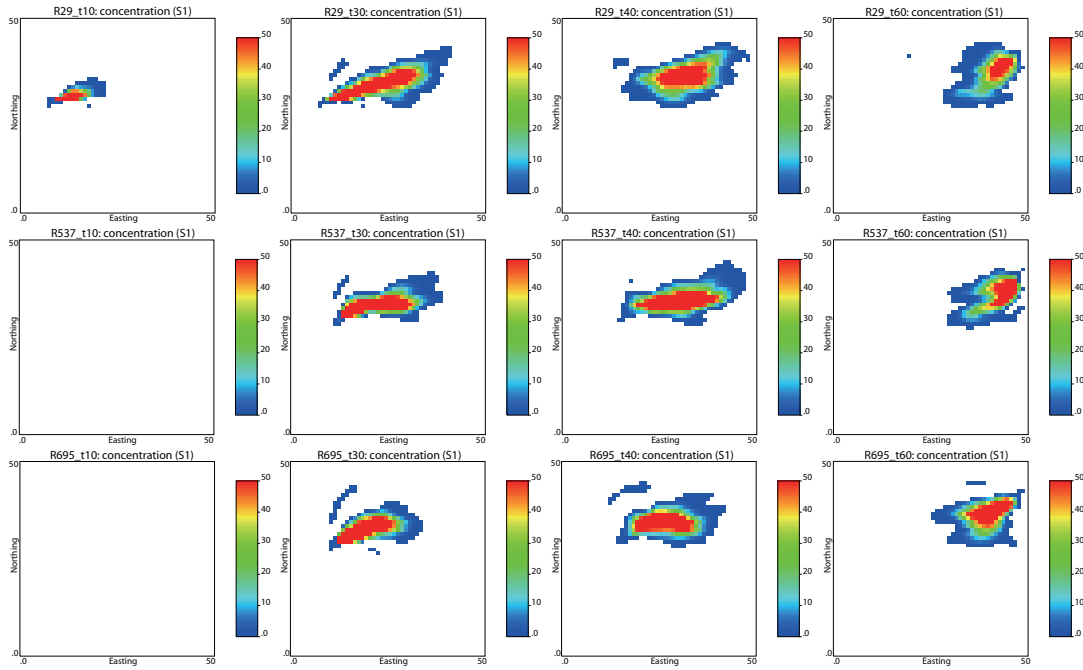


Figure 12: Scenario S1. Contaminant plume evolution of the 29th (top row), 537th (middle row), 695th (bottom row) realizations at the 10th, 30th, 40th and 60th time steps with the parameters updated after the 60th time step.

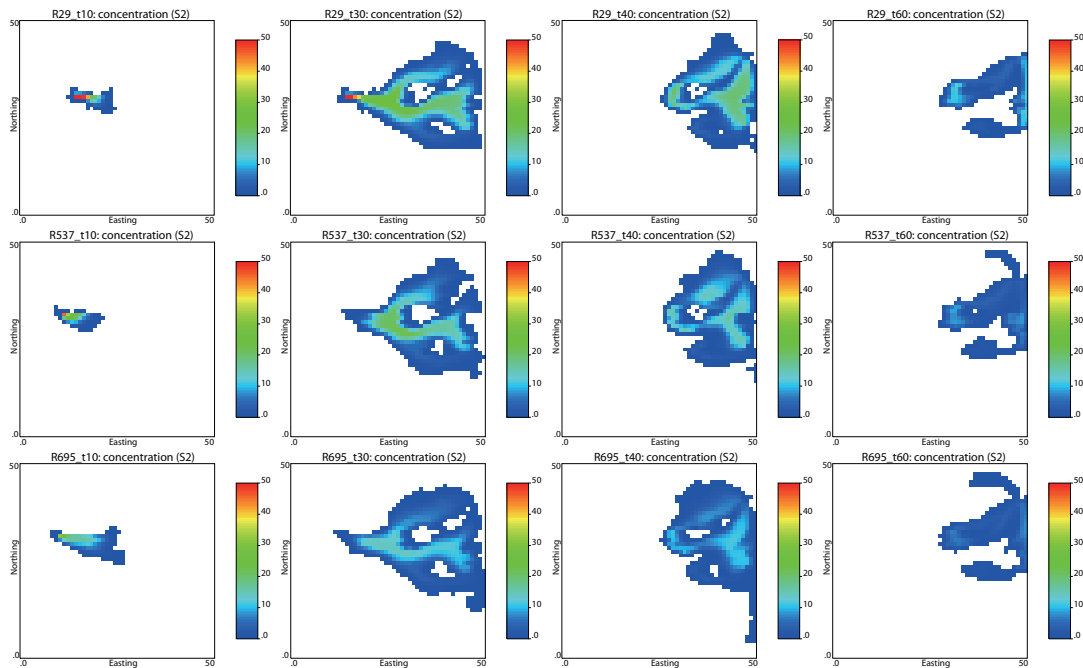


Figure 13: Scenario S2. Contaminant plume evolution of the 29th (top row), 537th (middle row), 695th (bottom row) realizations at the 10th, 30th, 40th and 60th time steps with the parameters updated after the 60th time step.

1712
 1713
 1714
 1715
 1716
 1717
 1718
 1719
 1720
 1721
 1722
 1723
 1724
 1725
 1726
 1727
 1728
 1729
 1730
 1731
 1732
 1733
 1734
 1735
 1736
 1737
 1738
 1739
 1740
 1741
 1742
 1743
 1744
 1745
 1746
 1747
 1748
 1749
 1750
 1751
 1752
 1753
 1754
 1755
 1756
 1757
 1758
 1759
 1760
 1761
 1762
 1763
 1764
 1765
 1766
 1767
 1768
 1769
 1770

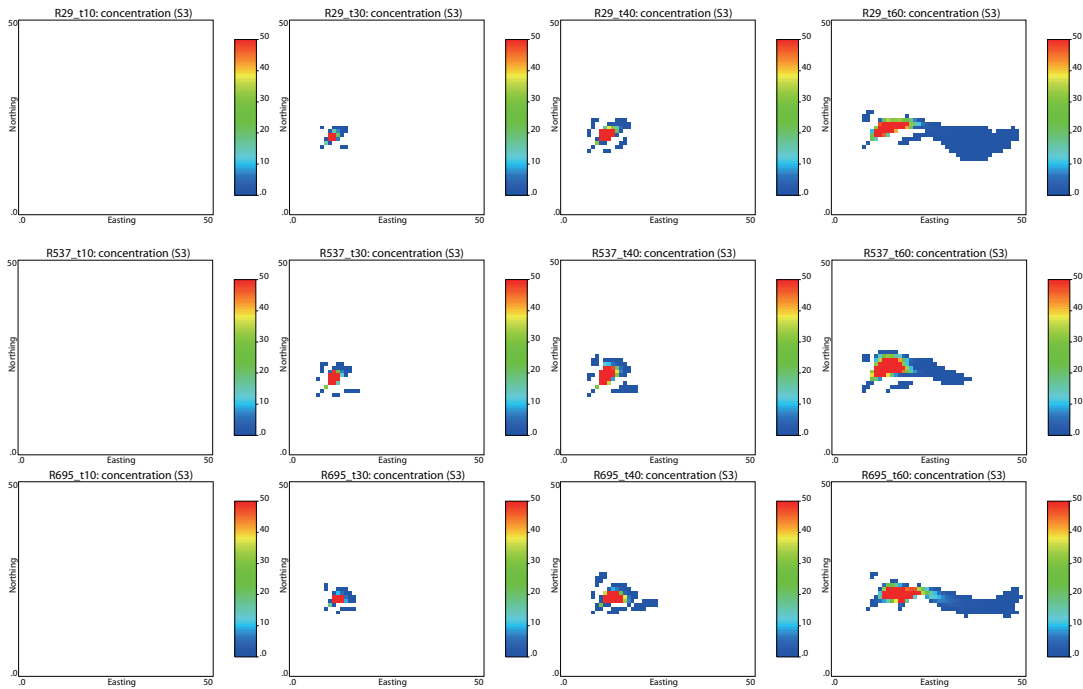


Figure 14: Scenario S3. Contaminant plume evolution of the 29th (top row), 537th (middle row), 695th (bottom row) realizations at the 10th, 30th, 40th and 60th time steps with the parameters updated after the 60th time step.

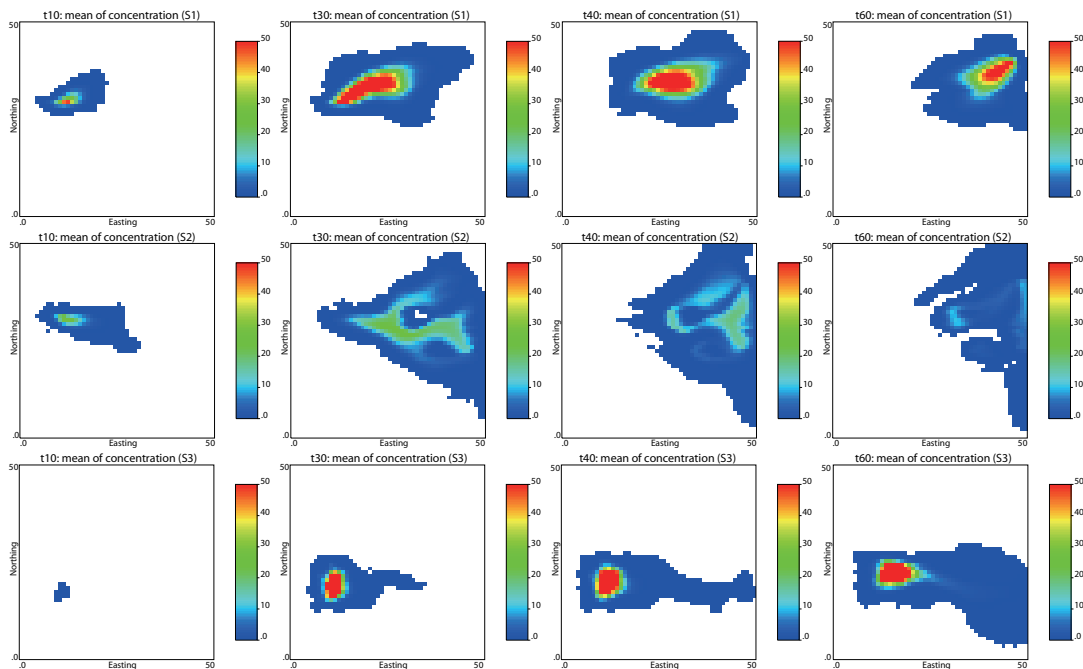


Figure 15: Scenarios S1-S3. Ensemble mean of contaminant plume evolution at the 10th, 30th, 40th and 60th time steps with the parameters updated after the 60th time step.

1771
 1772
 1773
 1774
 1775
 1776
 1777
 1778
 1779
 1780
 1781
 1782
 1783
 1784
 1785
 1786
 1787
 1788
 1789
 1790
 1791
 1792
 1793
 1794
 1795
 1796
 1797
 1798
 1799
 1800
 1801
 1802
 1803
 1804
 1805
 1806
 1807
 1808
 1809
 1810
 1811
 1812
 1813
 1814
 1815
 1816
 1817
 1818
 1819
 1820
 1821
 1822
 1823
 1824
 1825
 1826
 1827
 1828
 1829

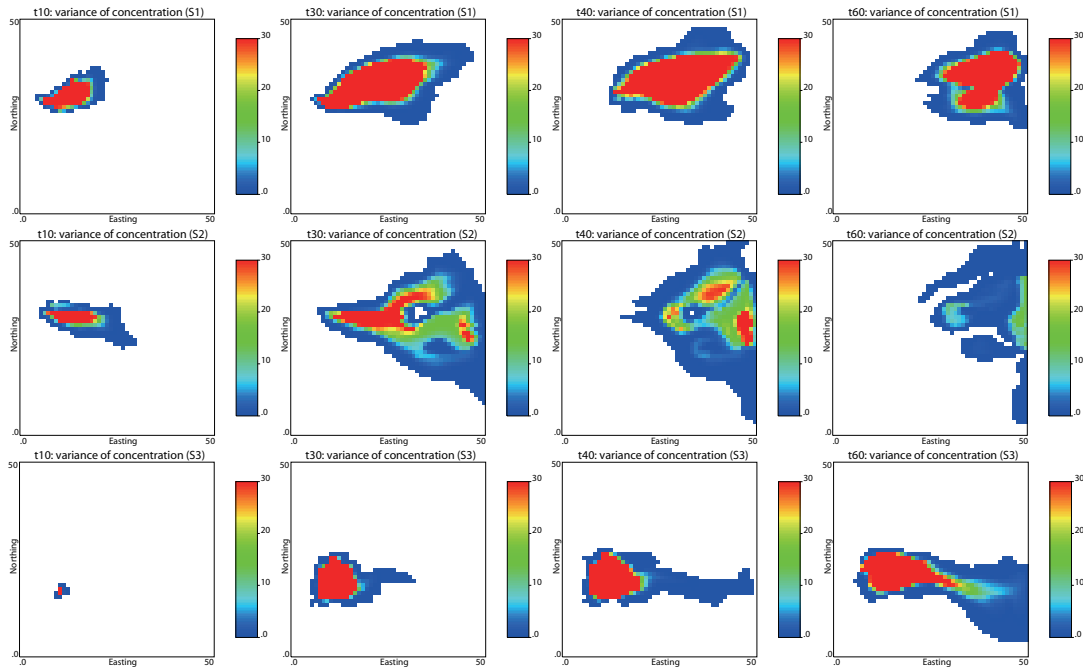


Figure 16: Scenarios S1-S3. Ensemble variance of contaminant plume evolution at the 10th, 30th, 40th and 60th time steps with the parameters updated after the 60th time step.

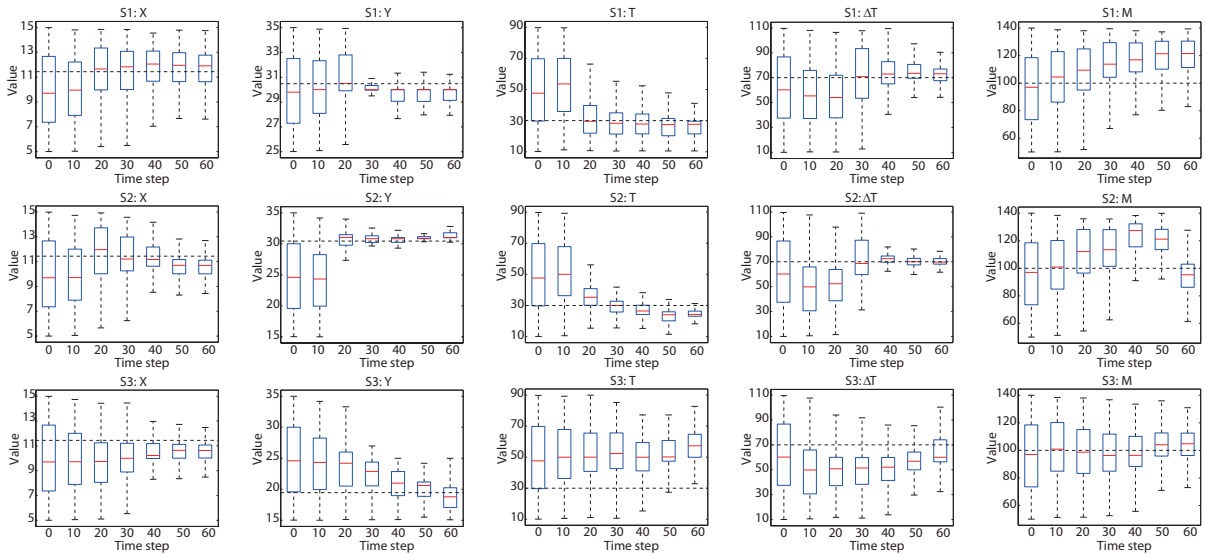


Figure 17: Scenarios S1-S3. Box plots of the source location coordinates (X and Y), initial release time (T), release duration (ΔT), and mass-loading rate (M) at the initial, 10th (30.68 [T]), 20th (64.57 [T]), 30th (102.02 [T]), 40th (143.38 [T]), 50th (189.06 [T]) and 60th (239.53 [T]) time steps. The dashed horizontal black line corresponds to the reference value.

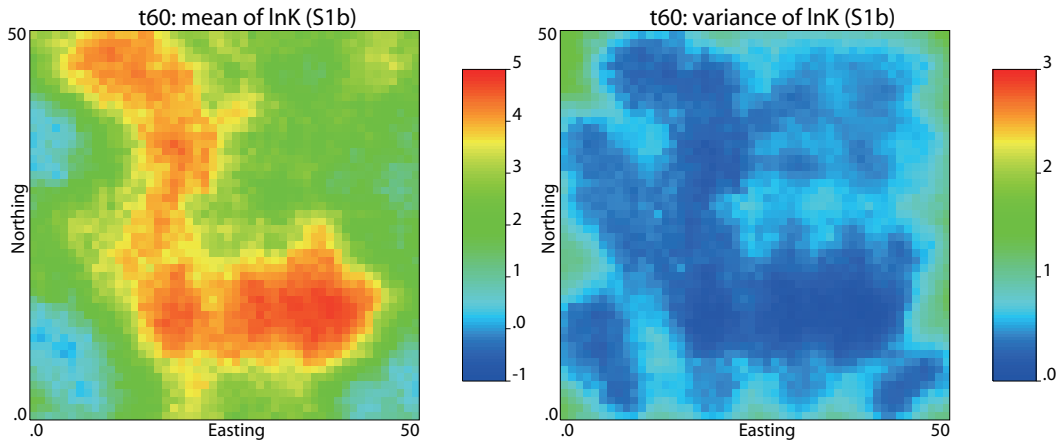


Figure 18: Scenario S1b. Updated ensemble mean (left column) and updated ensemble variance (right column) of $\ln K$ after the 60th time step.

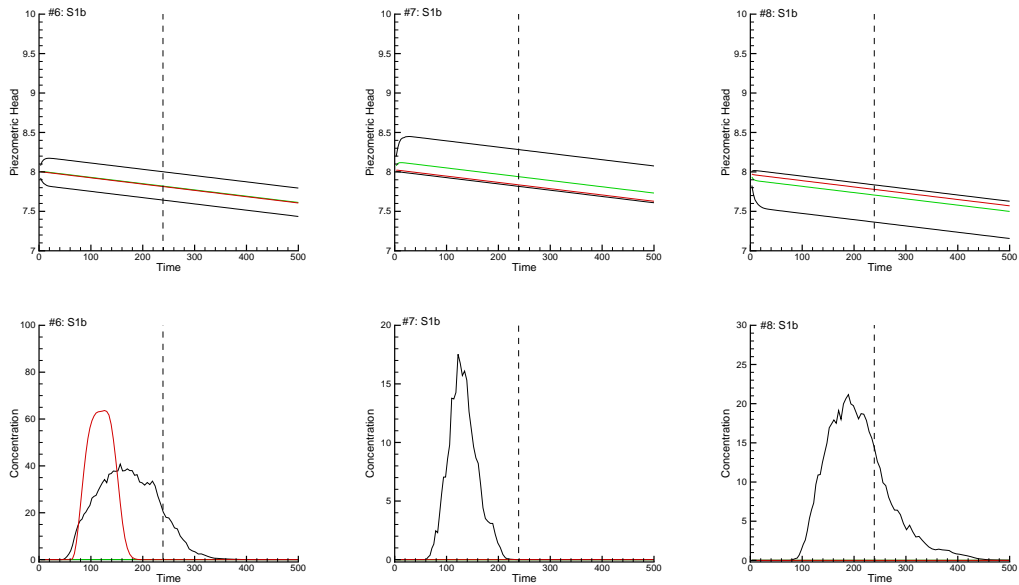


Figure 19: Scenario S1b. Time evolution of the piezometric heads (top row) and solute concentrations (bottom row) at the three wells #6, #7 and #8 for the initial ensemble of source information parameters and $\ln K$. The red line is the evolution of the piezometric head in the reference. The black lines correspond to the 5 and 95 percentiles of all realizations, and the green line corresponds to the median. The vertical dashed lines mark the end of the assimilation period.

1889
 1890
 1891
 1892
 1893
 1894
 1895
 1896
 1897
 1898
 1899
 1900
 1901
 1902
 1903
 1904
 1905
 1906
 1907
 1908
 1909
 1910
 1911
 1912
 1913
 1914
 1915
 1916
 1917
 1918
 1919
 1920
 1921
 1922
 1923
 1924
 1925
 1926
 1927
 1928
 1929
 1930
 1931
 1932
 1933
 1934
 1935
 1936
 1937
 1938
 1939
 1940
 1941
 1942
 1943
 1944
 1945
 1946
 1947

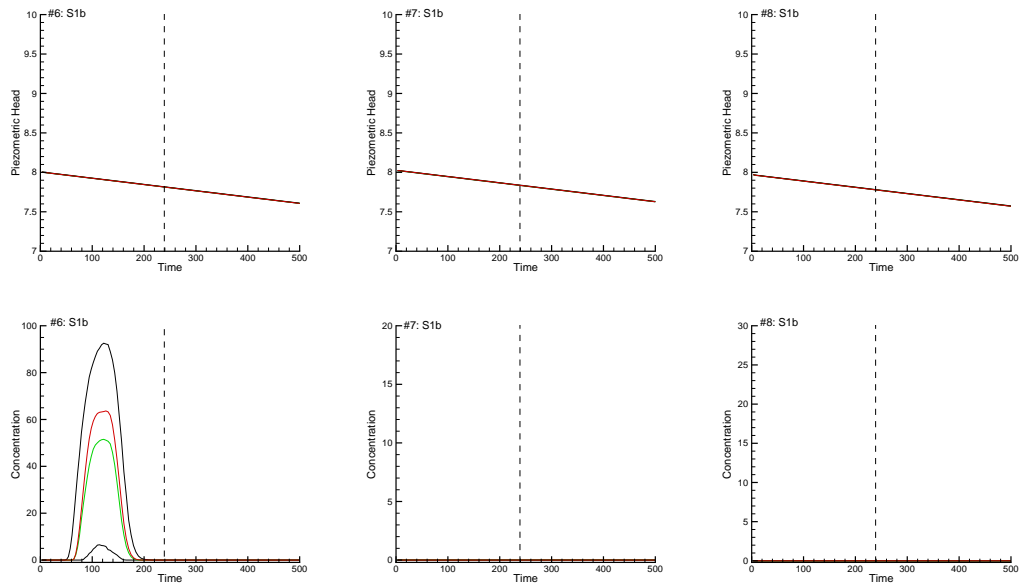


Figure 20: Scenario S1b. Same caption as previous figure but regarding piezometric heads and concentrations computed on the updated ensembles after the 60th assimilation time step.

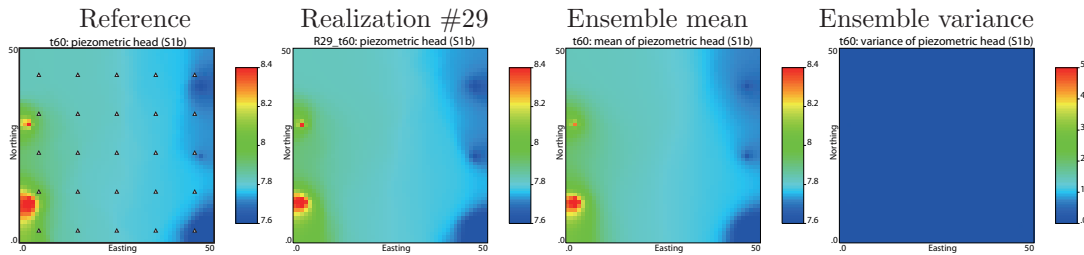


Figure 21: Scenario S1b. Piezometric heads at the end of the 60th time step. From left to right, heads in the reference aquifer; heads in realization #29; ensemble mean, and ensemble variance. White triangles mark the measurement wells.

1948
1949
1950
1951
1952
1953
1954
1955
1956
1957
1958
1959
1960
1961
1962
1963
1964
1965
1966
1967
1968
1969
1970
1971
1972
1973
1974
1975
1976
1977
1978
1979
1980
1981
1982
1983
1984
1985
1986
1987
1988
1989
1990
1991
1992
1993
1994
1995
1996
1997
1998
1999
2000
2001
2002
2003
2004
2005
2006

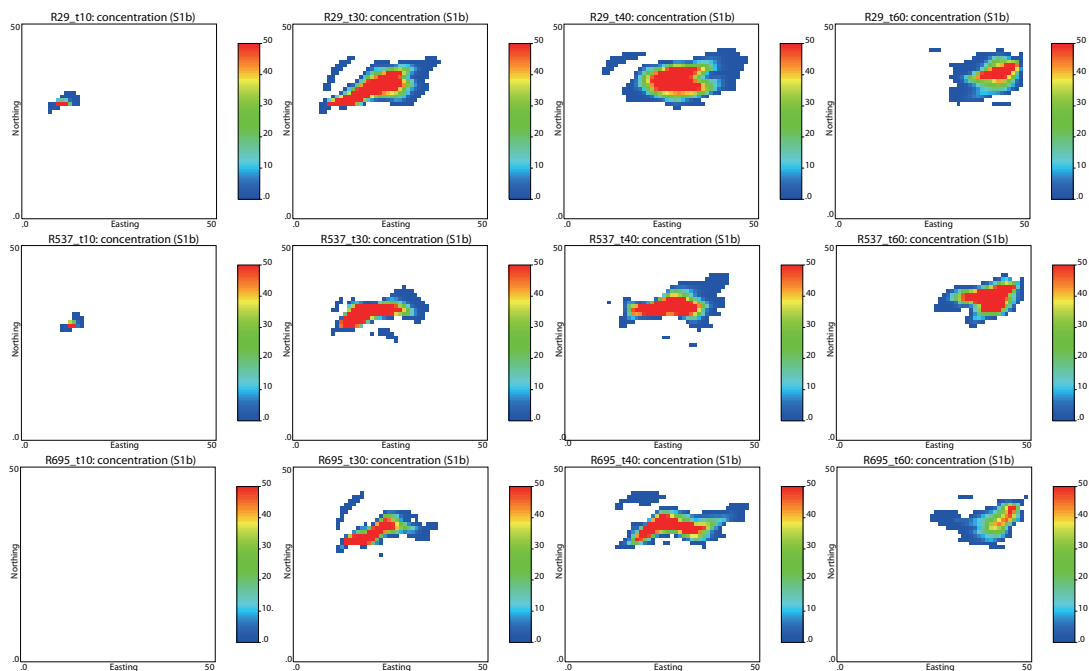


Figure 22: Scenario S1b. Contaminant plume evolution of the 29th (top row), 537th (middle row), 695th (bottom row) realizations at the 10th, 30th, 40th and 60th time steps with the parameters updated after the 60th time step.

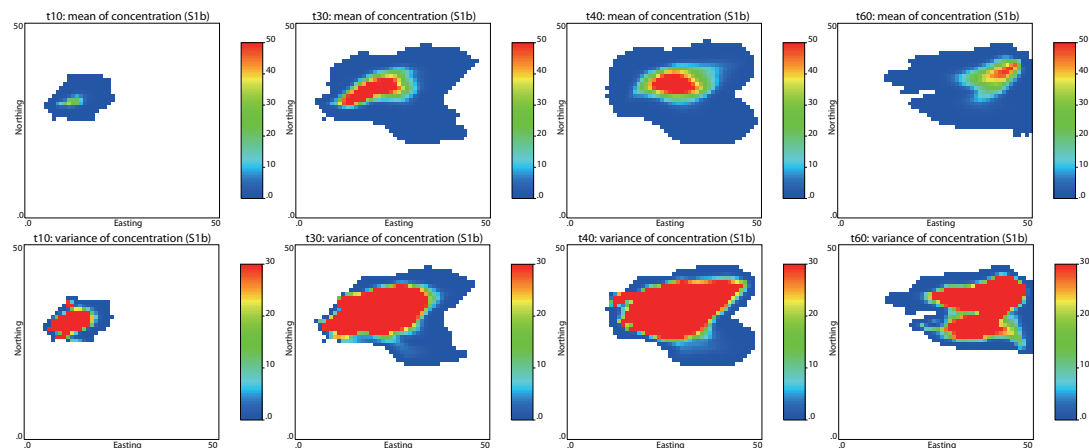


Figure 23: Scenarios S1b. Ensemble mean (top row) and ensemble variance (bottom row) of contaminant plume evolution at the 10th, 30th, 40th and 60th time steps with the parameters updated after the 60th time step.

2007
2008
2009
2010
2011
2012
2013
2014
2015
2016
2017
2018
2019
2020
2021
2022
2023
2024
2025
2026
2027
2028
2029
2030
2031
2032
2033
2034
2035
2036
2037
2038
2039
2040
2041
2042
2043
2044
2045
2046
2047
2048
2049
2050
2051
2052
2053
2054
2055
2056
2057
2058
2059
2060
2061
2062
2063
2064
2065

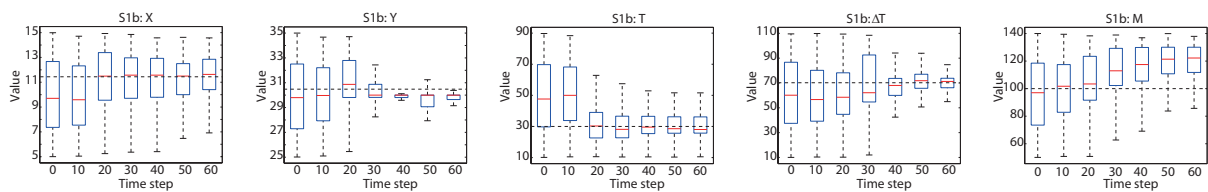


Figure 24: Scenarios S1b. Box plots of the source location (X and Y), initial release time (T), release duration (ΔT), and mass-loading rate (M) at the initial, 10th, 20th, 30th, 40th, 50th and 60th time steps. The dashed horizontal black line corresponds to the reference value.